5-2022

An Experimentally Validated Finite Element Model of Thermal Transient Response of a Railroad Bearing Adapter

Javier E. Arroyo
The University of Texas Rio Grande Valley

AN EXPERIMENTALLY VALIDATED FINITE ELEMENT MODEL OF THERMAL TRANSIENT RESPONSE OF A RAILROAD BEARING ADAPTER

A Thesis

by

JAVIER E. ARROYO

Submitted in partial fulfillment of the

Requirements for the degree of

MASTER OF SCIENCE IN ENGINEERING

Major Subject: Mechanical Engineering

The University of Texas Rio Grande Valley

May 2022

AN EXPERIMENTALLY VALIDATED FINITE ELEMENT MODEL OF THERMAL

TRANSIENT RESPONSE OF A RAILROAD BEARING ADAPTER

A Thesis
by
JAVIER E. ARROYO

COMMITTEE MEMBERS

Dr. Constantine Tarawneh
Chair of Committee

Dr. Arturo Fuentes
Committee Member

Dr. Stephen Crown
Committee Member

May 2022

ABSTRACT

Arroyo, Javier E., An Experimentally Validated Finite Element Model of Thermal Transient Response of a Railroad Bearing Adapter. Master of Science in Engineering (MSE), May, 2022, 101 pp., 37 tables, 33 figures, references, 16 titles.

Wayside hot box detectors (HBDs) are devices used to determine the health of railcar components such as bearings, axles, and brakes by monitoring the radiated temperature form these components. HBDs have been instrumental in reducing rail derailments in the decade, but the number of non-verified bearing removals has increased significantly. To combat these limitations, researchers have opted to use wireless onboard sensor devices directly mounted on the bearing adapter. The wireless onboard health monitoring system developed by the University Transportation Center for Railway Safety (UTCRS) utilizes temperature and vibration sensors to detect the condition of rolling stock. However, because the sensor is affixed to the bearing adapter, a transient thermal analysis was performed to determine the lumped capacitance behavior and the corresponding thermal lag of a railroad bearing adapter. To fully understand the heat transfer distribution, a finite element model (FEM) was developed to observe the thermal dissipation among the components. To validate the results, experimental data and the finite element simulation were compared against each other. These results can be used to identify the optimal anchor points for the temperature sensors on the bearing adapter and increase the proficiency of wireless onboard sensor devices in detecting defective components.

DEDICATION

This thesis is dedicated to my loving family and to all the friends I have had the honor of meeting throughout the years. My father, Javier, for inspiring and supporting me in my engineering career. My mother, Ruth, for always offering love and support. I would not be here or be the person who I am without you.

ACKNOWLEDGMENTS

I am truly grateful for my research advisor and mentor Dr. Constantine Tarawneh. Thank you for giving me the opportunity of joining your research team as a freshman. You have invested so much time and effort towards your student's success and walk them through their career goals. You have always pushed me to become the best engineer possible that I could ever be. I have learned so much from you and how to become a leader who leads by example. Words cannot express how grateful I am that we worked and collaborated for almost 6 years of my life.

I want to thank Dr. Arturo Fuentes for sparking my interest in finite element analysis and always to think outside the box. Thank you for your infinite input towards this work and my education. Without your guidance and support I would not be able to finish and fully understand this project.

Additionally, I would like to thank James, Joseph, Oscar and Anthony for teaching everything I know. Thank you all for you for answering my questions about modeling and technical issues that I had encountered. Without your patience and constant support, I would not be on the same level that I am right now. Thank you to everyone that welcomed me to the UTCRS, from the ones who have parted to the ones that are still here. To my current team, thank you for your hard work and support. Your time has come to navigate and keep in float the UTCRS ship. It has been an honor and great privilege to work and learn from every single one of you. Thank you, guys!

TABLE OF CONTENTS

Page

LIST OF TABLES

Page

LIST OF FIGURES

Page

CHAPTER I

BACKGROUND AND THEORY

1.1 Introduction

One of the leading mechanical causes of derailments in the rail industry is bearing failure. If the bearing fails, it may lock onto the axle causing failure of the railcar suspension system, which may lead to a catastrophic derailment. The suspension system of a freight railcar consists of the wheelset (wheel and axle), side frame, bearing adapter, roller bearing, and other main components as shown in Figure 1. As a result of the heavy cargo loads and relatively high operational speeds that railcars experience in service, the tapered roller bearings are the component most susceptible to failure.

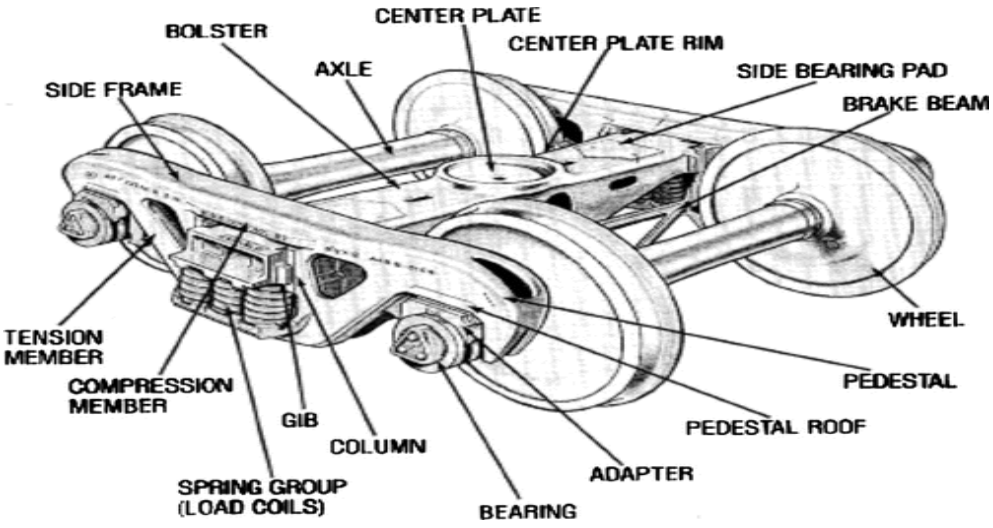

Figure 1: Freight Train Suspension [1]

The tapered roller bearing used in freight railcar service has three fundamental components: outer ring (cup), inner ring (cone), and rollers. These three fundamental components, depicted in Figure 2, allow near frictionless operation under high speeds and cargo load scenarios. However, due to the high speeds and high loading conditions, a defect may develop due to rolling contact fatigue (RCF), which can alter the effectiveness of near frictionless rotation of the rolling components. The latter will potentially lead to increased frictional heating between the bearing fundamental components.

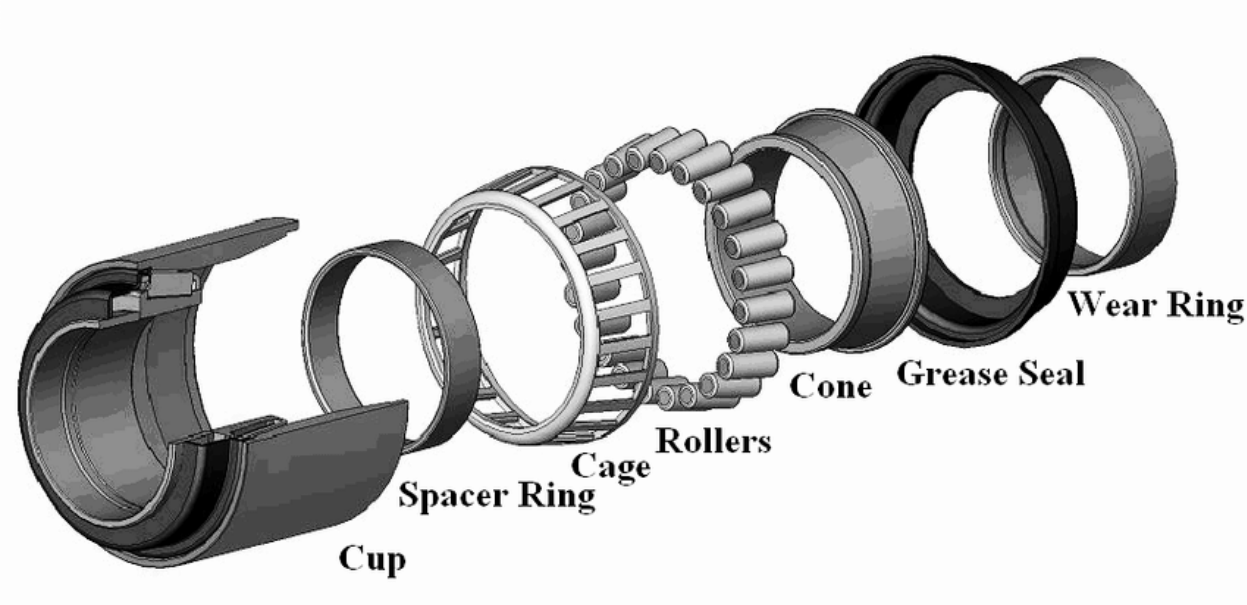

Figure 2: Tapered-Roller Bearing Exploded View [2]

Tapered roller bearing defects are generally classified in three different categories: geometric defects, localized defect, or distributed defects. A geometric defect, as the name implies, is when one or more of the bearing components is out of tolerance due to inconsistencies in the manufacturing processes. Examples of localized defects include pitting, cracks and/or spalls present on one of the three fundamental bearing components, as pictured in Figure 3. A distributed defect is when multiple bearing components have localized defects or a single bearing

component experiences multiple defects that are distribute throughout its rolling contact surface, such as “growler” illustrated in Figure 3. If not identified and removed from service, these defects will continue to deteriorate and generate excessive heating that raises the bearing operating temperature and may eventually lead to bearing burn-offs. On average, a bearing can burn off in a span of 1 to 3 minutes [3].

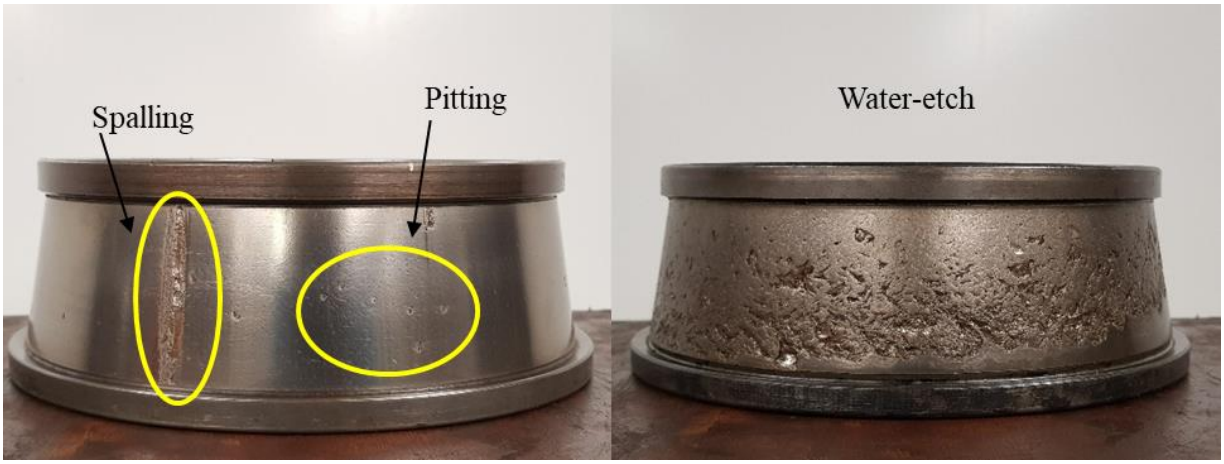

Figure 3: Example of a Localized Defect (Left) and a Distributed Defect (Right)

1.2 Wayside Detection Systems

The railroad industry currently utilizes two different types of wayside detection systems to monitor the health of tapered-roller bearings in service, namely: the Trackside Acoustic Detection Systems (TADS^{TM}) and the Hot-Box Detectors (HBDs) which come with Hot Wheel Detectors (HWD). However, these systems come with limitation that can lead to bearings being flagged incorrectly resulting in costly delays due to unnecessary train stoppages. With bearing failures being responsible for approximately 20% of the 800-million-wheel removals in North America, annually, this issue is too prevalent to depend on a system with reduced reliability [3].

1.2.1 Track side Acoustic Detection Systems (TADS^{TM})

As shown in Figure 4, the TADS^{TM} consists of multiple microphone arrays that span approximately 7.62 meters (25 feet) along the track. These arrays are strategically positioned on both sides of the track, at approximately the height of the railcar bearings. This type of system is commonly installed on tangent track, where the minimum speed of passing trains is 64km/h (40mph). Additionally, the system is not placed where trains have the need to apply the brakes, so as to reduce the interference associated with the brake noise that may lead to false positives [4]. TADS^{TM} is proficient in detecting high risk defects (i.e., growlers), in cups (outer rings), cones (inner rings), and roller, and loose cones. However, these are two downsides to this system; first, growlers is a bearing component containing defects that cover 90% or more of the component's rolling raceway area, and second, there are less than 30 of these systems installed in North America, with the majority of the systems located near the east coast. Hence, many bearings can go their entire service life without passing through any of these systems, and bearings with relatively small spalls or defects can go undetected even if the pass by one of these systems.

Figure 4: Photograph of a TADS™ site [5].

1.2.2 Hot-Box Detectors (HBDs)

HBDs use non-contact infrared sensors to measure the temperature radiated from the wheel-axle assemblies as they roll over the detector. A visual representation is depicted in Figure 5. HBDs alert the train operator when any bearings operate at a temperature that is 94.4°C (170°F) greater than the ambient temperature or 52.8°C (95°F) greater than the temperature of the mate bearing that shares the same axle [6]. However, many railroads have opted to use data acquired from HBDs to identify bearings operating at temperatures that are statistically higher than the average of all bearing temperatures on the same side of the train [7]. These bearings, which are referred to as “warm-trending” bearings, are removed from service, and sent to specialized facilities for disassembly and inspection. In most cases, bearing overheating can occur due to one or more of the following reasons: spalling, loose components, water contamination, broken components, damaged seals, or roller misalignment. Upon inspection, if the bearings do not exhibit any visible signs of damage or defects, they are classified as “nonverified”.

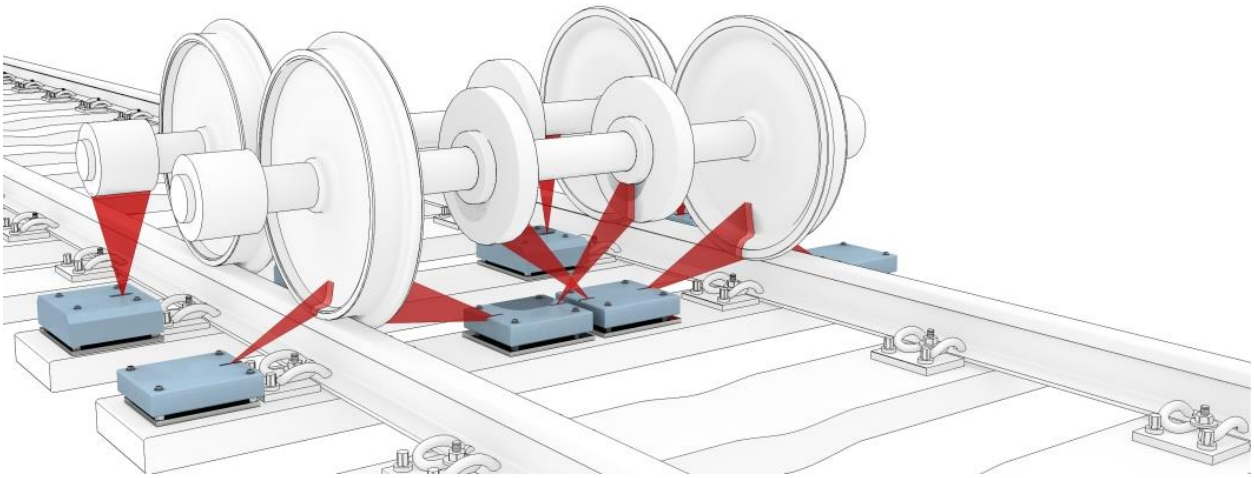

Figure 5: HBD CAD Model [8]

HBDs are sparsely installed across North America, which one is of their limiting factors. The North American railroads have installed around 6,000 HBDs throughout their network and placed them every 40-rail km (25 miles) to 64-rail km (40 miles) on average [9]. As previously mentioned, a bearing burnout usually occurs in less than 3 minutes. Hence, a freight car traveling at a leisurely 72 km/h would see the bearing fail over the course of 3.6 km (2.24 miles). Meaning that, HBD are too few and far between to be able to proactively detect bearing failures. Detection is further hampered by several factors including environmental conditions, railroad bearing class which determines bearing position on the axle relative to the wayside detector sensor location, surface conditions of the bearing cups (outer rings), and train speed as it passes over the HBDs. Moreover, several laboratory and field studies have indicated that the accuracy and reliability of the HBD temperature readings are inconsistent [8].

To combat these limitations, researchers at the University Transportation Center for Railway Safety (UTCRS) have opted to use wireless onboard sensors devices mounted directly on the railroad bearing adapter, as illustrated in Figure 6. These onboard health monitoring system collects and analyzes both the temperature and the vibration profiles of the railroad

bearing. However, these wireless onboard condition monitoring systems predicts the bearing operating temperature indirectly from their affixed position on the bearing adapter instead of reading the actual bearing surface temperature. This process introduces a thermal time lag between measured and actual bearing operating temperature.

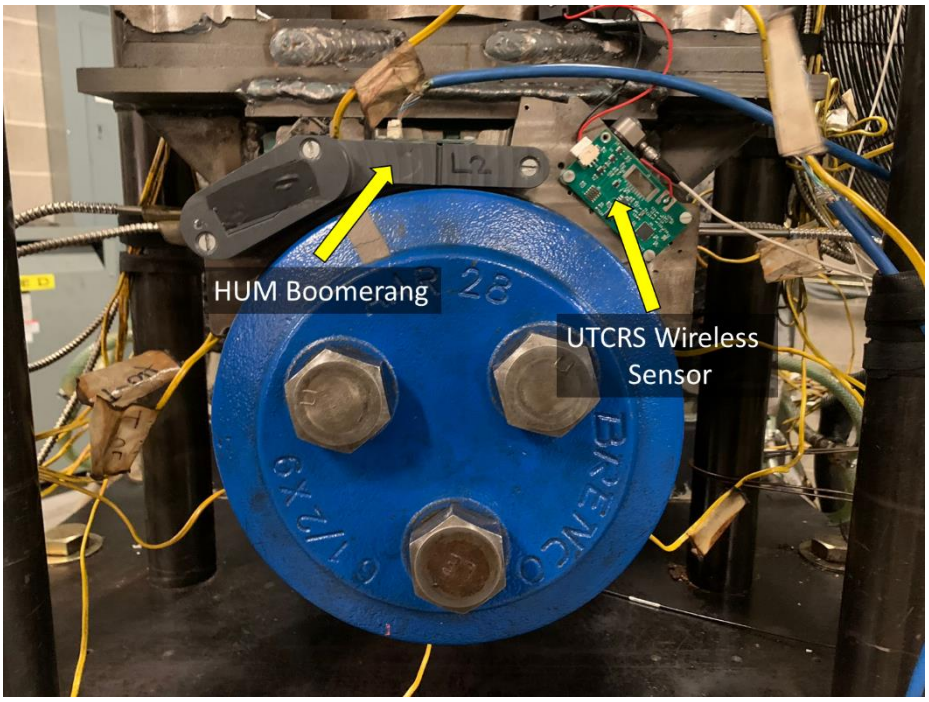

Figure 6: Wireless Onboard Condition Monitoring Sensors

To understand this thermal response of the bearing adapter and quantify the thermal lag, a transient heat transfer finite element model (FEM) was developed and used to perform numerous simulations to obtain the thermal distribution throughout the bearing adapter to determine if it can be assumed as a lumped capacitance body. If true, the latter implies that the wireless onboard condition monitoring sensors can be placed anywhere the adapter geometry allows since the temperature will be evenly distributed around the bearing adapter. The finite element analysis (FEA) simulations were compared against operating temperature data acquired from experiments

conducted on the UTCRS dynamic test rigs to validate the accuracy and reliability of the simulation results.

The work presented in this thesis will focus on the following three major outcomes:

(1) Developing an experimentally validated, accurate, and reliable finite element model for the transient thermal response of railroad bearing adapter.

(2) Obtaining the thermal distribution maps within the railroad adapter through FEA at different operating conditions, and providing heat transfer systematic calculations to determine whether the bearing adapter can be assumed as a lumped capacitance body.

(3) Quantifying the thermal lag between the bearing adapter and the adapter by acquiring the time constants for several bearing operating scenarios taking into account varying speed and load operating conditions.

Previous work performed on railroad bearings and adapters utilizing FEA modeling is provided in Chapter II. Heat transfer analytical calculations are presented in Chapter III. In Chapter IV, a detailed description is provided of the developed finite element model and its boundary and initial conditions, and the dynamic bearing test rigs used to conduct the experimental validation testing for this study. Chapter V presents the results of the experimental testing and the FEA simulations carried out under different load and speed operating scenarios. Finally, Chapter VI discusses the main findings of this thesis and the limitations of the developed model and suggests ways to improve the developed FEA model.

CHAPTER II

LITERATURE REVIEW

To fully comprehend the thermal heat distribution among the tapered roller bearing components during service operation, theoretical and numerical models, such as the Finite Element Model (FEM), are needed since analytical calculations have limitations and require simplified assumption.

Fortunately, a few FEMs have been developed to mimic field operating conditions through simulated laboratory setups. Tarawneh *et al.* [12], developed a FEM that was used to simulate the heat generation experienced by railroad bearings under several operating conditions. The main goal of the study was to investigate whether some rollers within the cone assembly can reach temperatures of 232°C (450°F) without raising the cup (outer ring) temperature to thresholds that would trigger a hot-box detector (HBD) alarm. The motivation behind the study was the discoloration (i.e., heat tint) observed on some of the rollers of nonverified bearing. Nonverified bearings are those that are flagged by HBDs because they exhibit warm trending events but, upon tear down and inspection, are found to have no discernable defects or damage.

Laboratory testing was performed utilizing a furnace to heat several rollers dipped in bearing grease to several elevated temperatures and observe any roller discoloration. Results indicated that the visual discoloration which best matched that observed in bearings removed from service were rollers heated in grease to temperatures over 232ºC (450ºF) for periods of at least 4 hours [10]. Additionally, static testing was conducted using cylindrical heaters embedded

in two rollers to better understand the heat transfer paths within the bearing assembly [11]. The data acquired from these experiments were used to quantify the overall heat transfer coefficients for the railroad class F and K bearings. The laboratory testing results helped inform the FEM that was developed for this particular study.

As stated earlier, the purpose of the devised model was to recreate operating conditions where certain rollers can get to elevated temperatures without raising the bearing operating temperature, especially the outer surface of the cup which is scanned by the infrared sensors, to levels that would trigger a hot-box detector (HBD) alarm. The model of the bearing assembly was generated utilizing a three-dimensional graphing software Pro/Engineering™ [12]. The axle was rendered as a cylinder with a diameter of 0.1572 m (6.1890 in) and a length of 2.2 m (86 in), which is enough length to act as a heatsink. The finite element model with its respective mesh is illustrated in Figure 7.

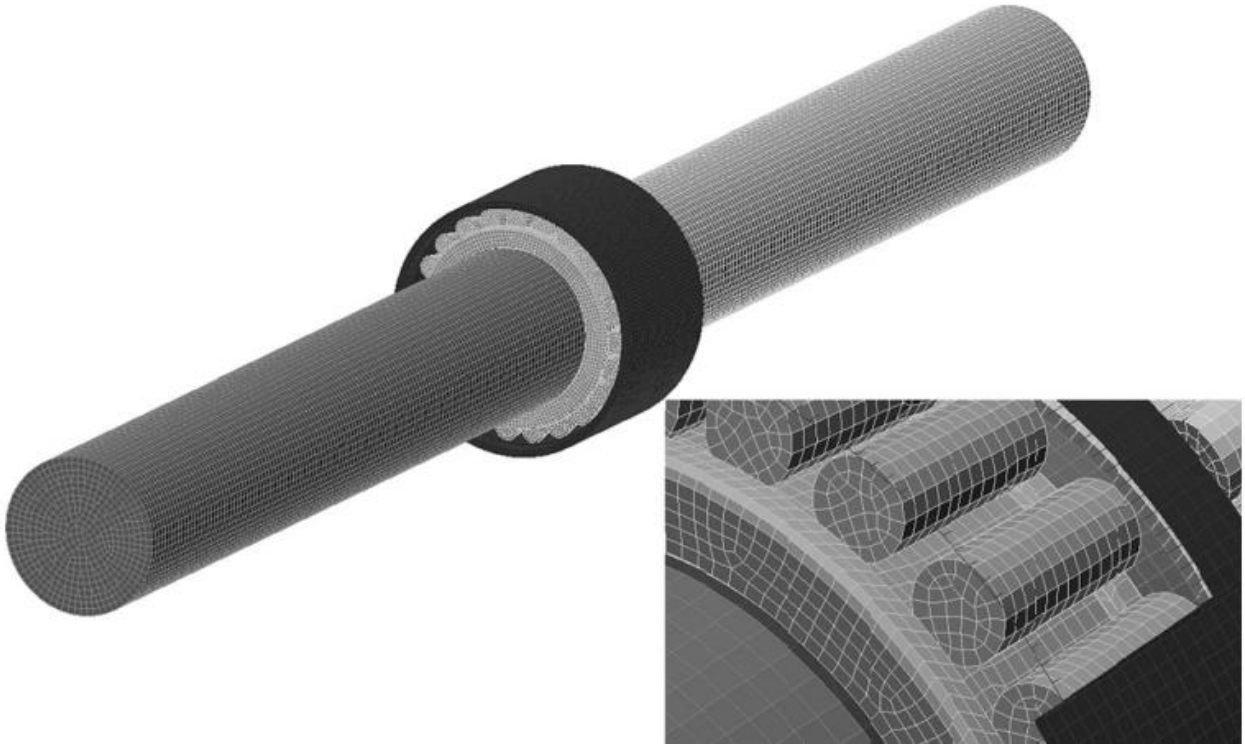

Figure 7: Finite Element Model Used for Study from Reference [12]

The bearing used in this study was modeled after a class K railroad tapered roller bearing with slight modifications for simplification purposes and to achieve faster computational responses. Some of the simplifications are the following: no cages, seals, wear rings, or grease were included due to thermal resistances of the polyamide cage and grease being large in comparison to the components of the bearing assembly, leading to most of the heat flowing through the rollers to the bearing cones (inner ring) and cup (outer ring). The wear rings are in contact with the axle, which constitutes a very large body of metal acting as a heatsink. So, omitting these components will not have a significant effect on the results acquired from the simulation [12]. Additionally, the bearing adapter was not modeled since the axle was long enough to act as a heatsink and the omission of this component will not affect the heat dissipation routes. Once the bearing and its components were created using the computer-aided

design (CAD) software, the CAD drawing was imported to the engineering software ALGOR 20.3^{TM} where the boundary conditions were applied, and the numerical simulations were run.

The boundary conditions applied to the FEM developed by Tarawneh *et al.* [12] were: AISI 8620 with a thermal conductivity of 46.6 $W \cdot m^{-1} \cdot K^{-1}$ for the bearing steel, and AISI 1060 with a thermal conductivity of 51.9 $W \cdot m^{-1} \cdot K^{-1}$ for the steel axle. From previous published work [11], an overall bearing cup heat transfer coefficient was found with a value of H_o = 8.32 $W \cdot K^{-1}$, which takes into consideration both forced convection induced by a 5 m/s airstream and radiation emitted to an ambient temperature of 25ºC (77ºF). To satisfy the software input for convection, the overall heat transfer coefficient was divided by the cup surface area of A_{cup} = 0.1262 m^2, leading to an overall convection coefficient of h_o = 65.9 $W \cdot m^{-2} \cdot K^{-1}$. The axle convection coefficient was calculated to be 25 $W \cdot m^{-1} \cdot K^{-1}$ using an air stream of 6 m/s and the same ambient temperature of 25ºC (77ºF). The boundary conditions were directly applied to the FEM as depicted in Figure 8.

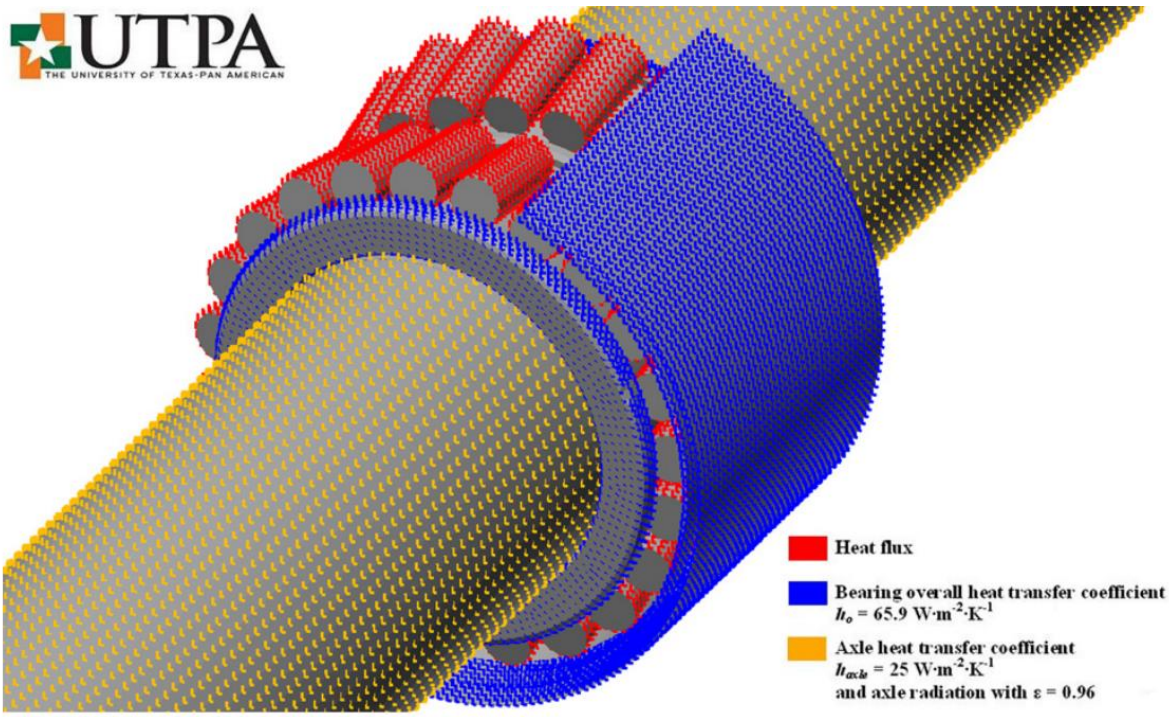

Figure 8: FEM Applied Boundary Conditions from Reference [12]

To verify the accuracy of the FEM, thirteen different heat generation scenarios were conducted and summarized in Reference [12]. From those thirteen cases, three cases (presented in Table 1) will be discussed for the sake of brevity. Case 1 describes a normal operating bearing where all 46 rollers were equally heated to achieve a temperature of 52ºC (125.6 ºF). The heat generation applied to each roller had a value of Q_{roller} = 11.5 W. In other words, this case mimics a healthy (control) bearing where no roller misalignments or defects are present on any of the components of the railroad bearing. The model used a steady-state simulation where time steps were not considered. The simulation results for this case showed an approximate average bearing temperature of 50.2ºC (122ºF) as depicted in Figure 9.

Table 1: Selected Heating Scenarios Used from Reference [12]

Case No.	Q_{total} (W)	Q_{roller} (W)	Maximum average roller temperature (ºC)	Average cup temperature (ºC)
1	529.0	11.5	55.0	50.2
2	1287.4	264.3	232	88.5
3	2208.0	48.0	149.5	130.5

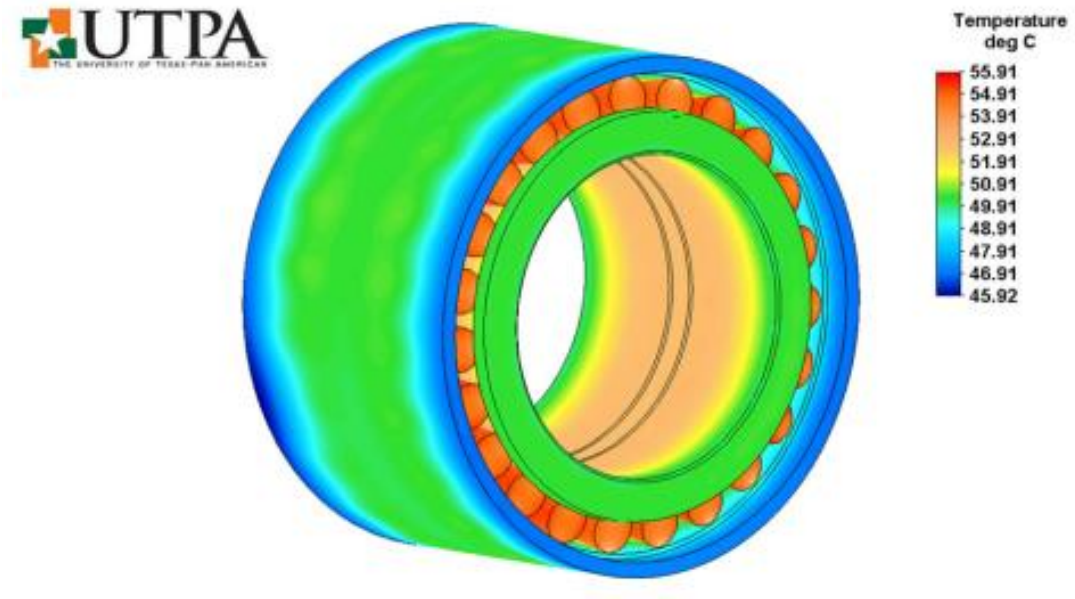

Figure 9: FE analysis results from Case 1 Used from Reference [12]

Case 2 introduces a scenario where three adjacent rollers were caught misaligned while entering the loaded zone. The remaining 43 rollers were operating normally, and thus had the same heat input as the rollers in Case 1. On the contrary, the three adjacent rollers that were caught misaligned generated excessive amounts of frictional heating, and therefore had a heat input of Q_{roller} = 264.3 W. This case replicates the behavior of a nonverified bearing, since the three roller temperatures reached 232ºC (450ºF) and will most likely exhibit the discoloration (heat tint) visually observed on rollers of nonverified bearings. The simulation results are

illustrated in Figure 10, where the bearing had an average cup temperature of 88.5ºC (191ºF), which is well below the HBD threshold and will continue to operate abnormally while undetected by conventional wayside detection systems. This simulation proved that it is possible for some rollers to reach elevated temperatures that can cause visible heat tinting without raising the bearing cup temperature to levels that would trigger an HBD alarm. Nevertheless, the bearing cup temperature of 88.5ºC is sufficient to categorize this bearing as one that is undergoing warm-trending, which will result in its removal from service and later labeled as nonverified.

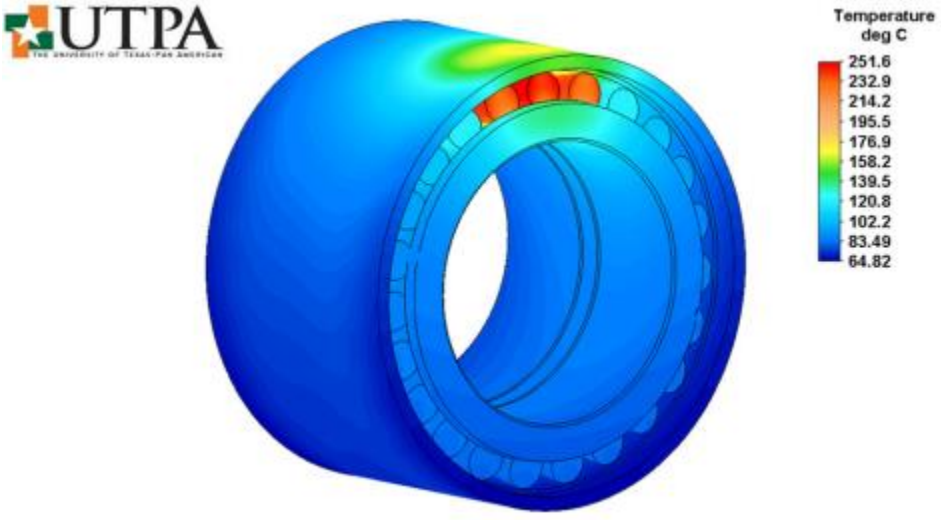

Figure 10: FE Analysis Results from Case 2 Used from Reference [12]

Lastly, Case 3, illustrated in Figure 11, represents a bearing operating abnormally with all its rollers caught misaligned generating a heat input per roller of Q_{roller} = 48.0 W. The corresponding bearing cup temperature for this case is 130.5ºC (267ºF), which introduces an operating bearing condition that will trigger a hot-box detector (HBD) alarm. For this case, the temperature of the rollers, as given by the FEM simulation, is about 149.5ºC (301ºF), which is valuable information considering that it is not feasible to obtain the actual temperatures of the internal components of the bearing while in operation. Hence, the proposed FEM is a tool that

can be used to circumvent the latter issue by providing reliable information about the bearing internal temperature distribution.

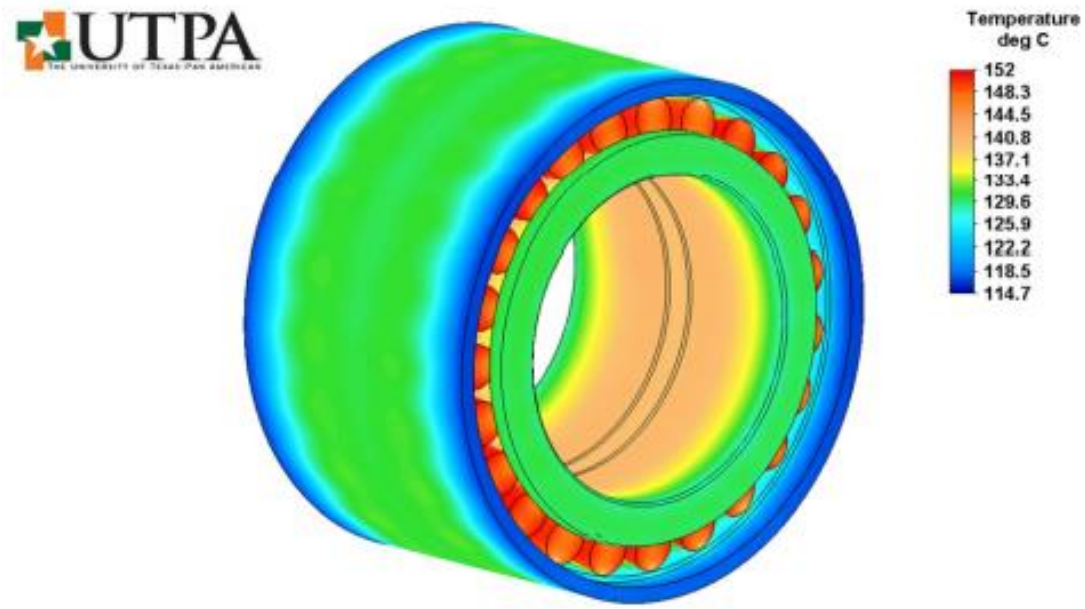

Figure 11: FE Analysis Results from Case 3 Used from Reference [12]

This FEM was only the first step towards fully understanding the thermal distribution of the heat generation within the railroad tapered-roller bearing assembly. One of the main drawbacks of this model was that it did not include the bearing adapter and the heat path to the side frame of the railcar.

To that end, Zagouris [14] created a FEM based on the one proposed by Tarawneh *et al.* [12] but including two types of bearing adapters: an all-steel adapter and an AdapterPlus™ containing a polymer steering pad. The addition of the bearing adapter and the polymer steering pad to the FEM was needed to calibrate Wireless Sensor Nodes (WSNs) developed by IONIX, LLC, a subsidiary of Amsted Rail. The system named IONIX EDGE™ was extensively tested

and validated by researchers from the University Transportation Center for Railway Safety (UTCRS) before being deployed in a field test in Australia [13]. Zagouris [14] developed a temperature correlation between the bearing adapter and the bearing cup (outer ring) to enhance the temperature readings of the IONIX EDGE™ [14]. Figure 12 shows a typical placement for an IONIX EDGE™ WSN on a conventional metal adapter for field applications.

Figure 12: IONIX EDGE™ WSN Placement

Zagouris [14] was able to calibrate the temperature correlations with experimental data acquired by utilizing different bearing classes, load scenarios, rail operating speeds, ambient temperatures, and bearing and adapter conditions. A thermal contact resistance between the bearing cup (outer ring) and the bearing adapter was found by conducting a pressure film test to

quantify the contact pressure between the abovementioned components [14], and then applied to the FEM. The thermal contact resistance will dictate the amount of heat transferred through the components. After applying the thermal contact resistance, the FEM simulations were run utilizing the engineering software ALGOR 20.3™, and the steady-state simulation results were compared to the experimental data acquired from running bearings on the UTCRS dynamic test rigs.

As mentioned earlier, the testing phase for the FEM was split to two models with slight modifications in the bearing adapter. A model with a conventional all-steel adapter was developed, shown in Figure 13, as well as second model with an AdapterPlus™, illustrated in Figure 14. The main difference between the adapters is the addition of the polymer steering pad, which partially insulates the adapter from the I-beam in the experimental setup. Additionally, the AdapterPlus™ has two copper studs in the polymer pad, which will create an additional thermal runaway. Another major difference is the length of the axle between both models, as depicted in Figure 13 and Figure 14. Figure 13 has a shorter axle which makes the I-beam act as heat sink, whereas Figure 14 has a longer axle which accounts for the insulating properties of the adapter polymer pad [14].

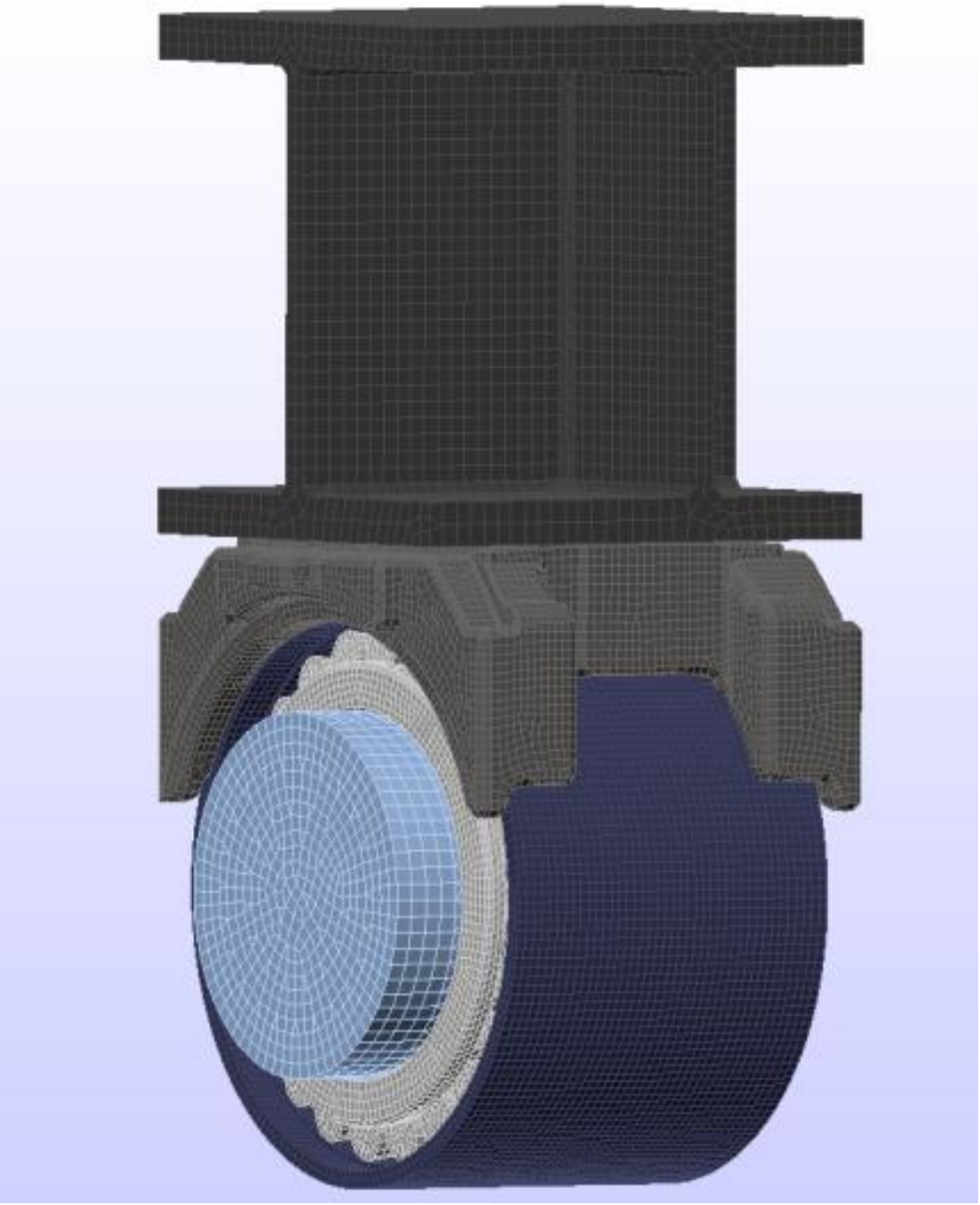

Figure 13: FEM with a Conventional Metal Adapter Used in Reference [14]

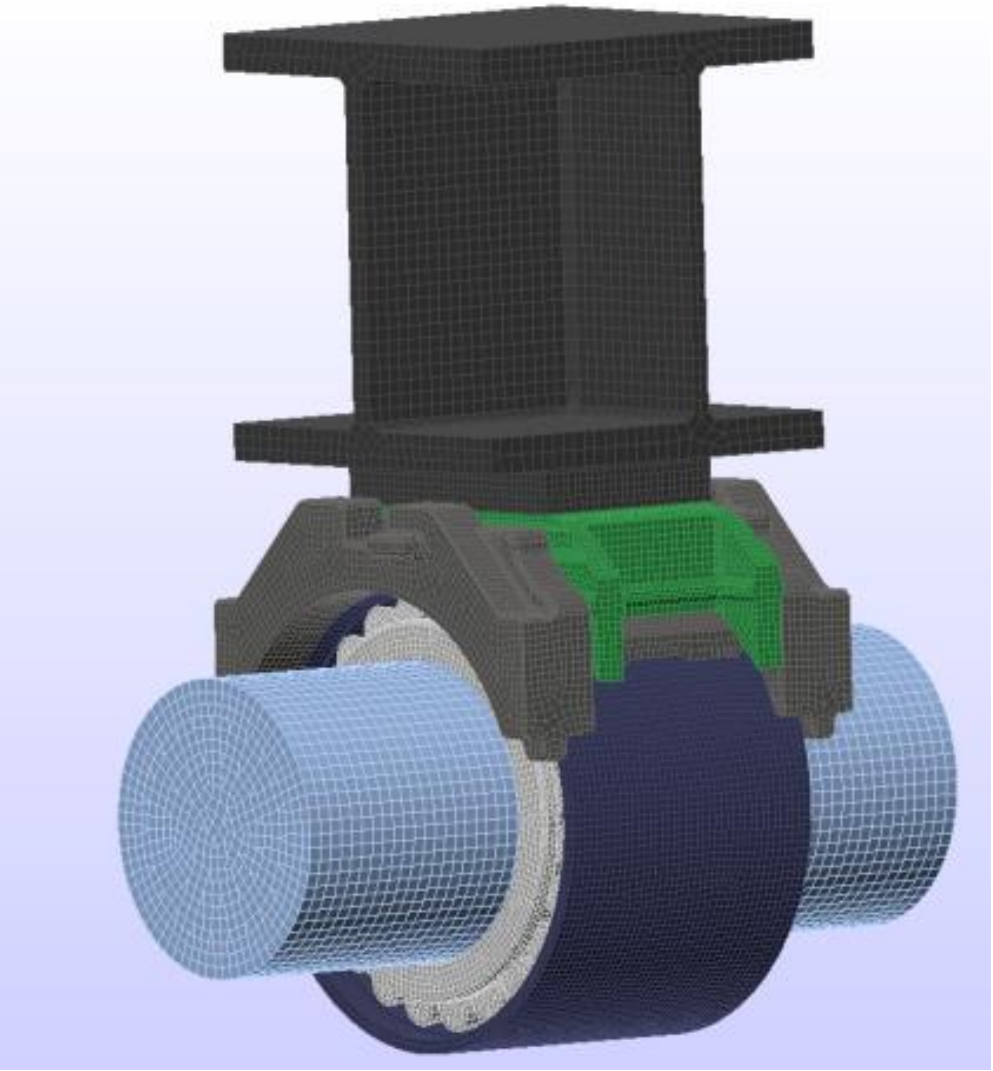

Figure 14: FEM with AdapterPlus^{TM} Used in Reference [14]

The boundary conditions for both models were acquired from Tarawneh *et al* [12] previous work. Ductile (nodular) iron, with a thermal conductivity of 34.4 $W \cdot m^{-1} \cdot K^{-1}$ was used for the bearing adapter material, and a thermal conductivity of 0.25 $W \cdot m^{-1} \cdot K^{-1}$, sourced from BASF literature for urethane and based on the Shore durometer, was used for the elastomer pad [14]. The elastomer pad carries two small copper pins that can transmit heat from the AdapterPlus^{TM} to the spacer plate and I-beam; a thermal conductivity value of 401 $W \cdot m^{-1} \cdot K^{-1}$ was applied to the copper pins [15].

The FEM was tested in two scenarios listed in Reference [12] namely, the normal operating bearing case and the abnormal operating case. The thermal contact resistance between the cup (outer ring) and the bearing adapter was optimized once the experimental and simulation adapter temperatures matched each other. The experimental temperature data was taken from the IONIX EDGE™ WSN, and the simulation data was taken from a node selection illustrated in Figure 15. The bearing model with the AdapterPlus™ was of greater interest since it is the modern adapter bound to replace the older all-steel conventional adapters.

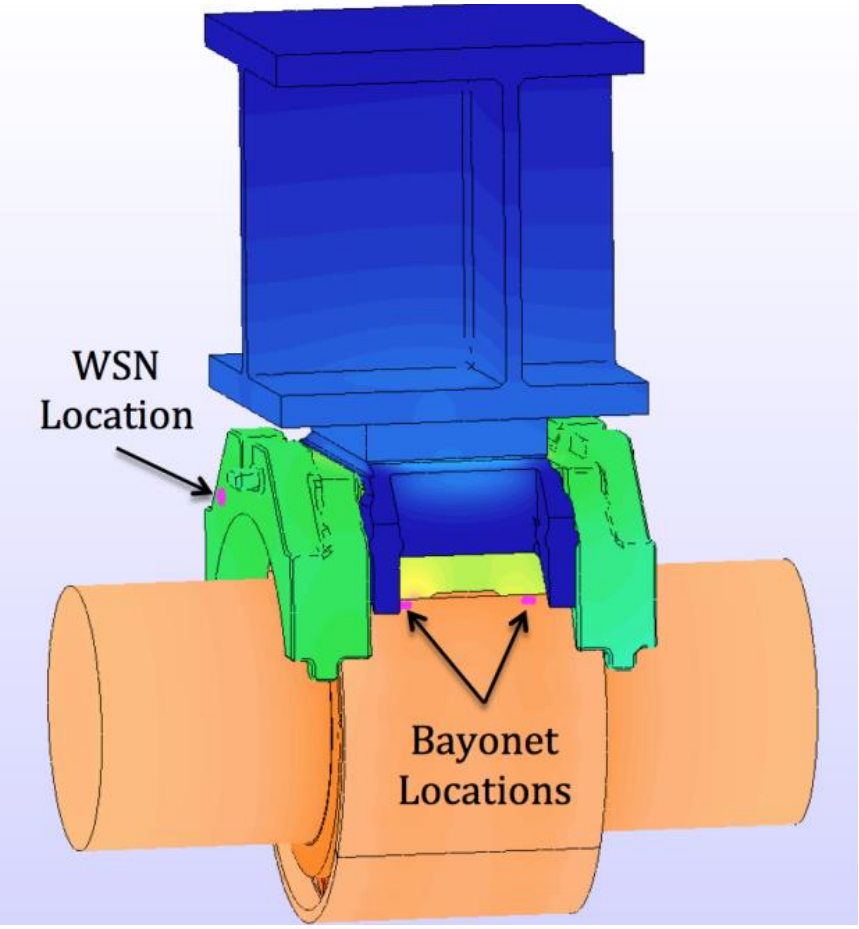

Figure 15: AdapterPlus™ FEM Node Selection [14]

The experimental data for normal operating conditions ran at 97 km/h (60 mph) with different ambient temperatures and loading scenarios. For the conventional adapter, the load was

set to simulate a fully loaded railcar (100%) with an ambient temperature of 22ºC (72ºF) and for the AdapterPlus™ setup, the load was set to 95% of a fully loaded railcar with an ambient temperature of 25.5ºC (78ºF). The abnormal case was tested at 135 km/h (84 mph) under a full railcar load (100% load) and an ambient temperature of 43.7ºC (111ºF). The test bearing was packed with extra grease to increase the heat generation rate within the bearing. The results for both models are comparable to the experimental data with a percent error of 3.1% and 8.8% for the conventional and AdapterPlus™ models, respectively.

For the normal operation case, the thermal resistance between the bearing cup and adapter, for both models, was quantified. For the conventional all-steel adapter and the AdapterPlus™ models, the thermal resistances were set to 0.006 $m^{2} \cdot K \cdot W^{-1}$ and 0.0055 $m^{2} \cdot K \cdot W^{-1}$, respectively. The values were experimentally validated by comparing the laboratory acquired steady state temperatures to the numerical simulation results illustrated in Figure 16 and Figure 17.

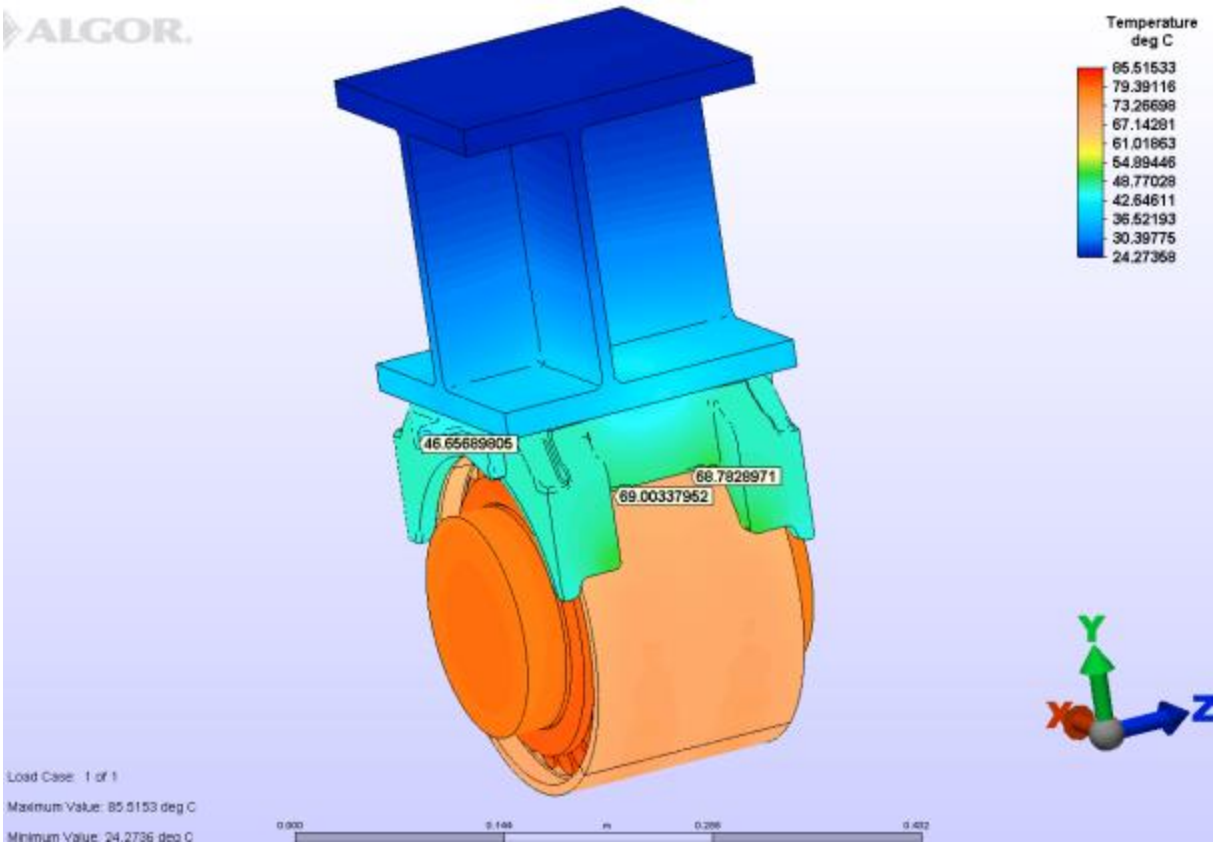

Figure 16: Conventional Adapter Temperature Distribution – Normal Case [14]

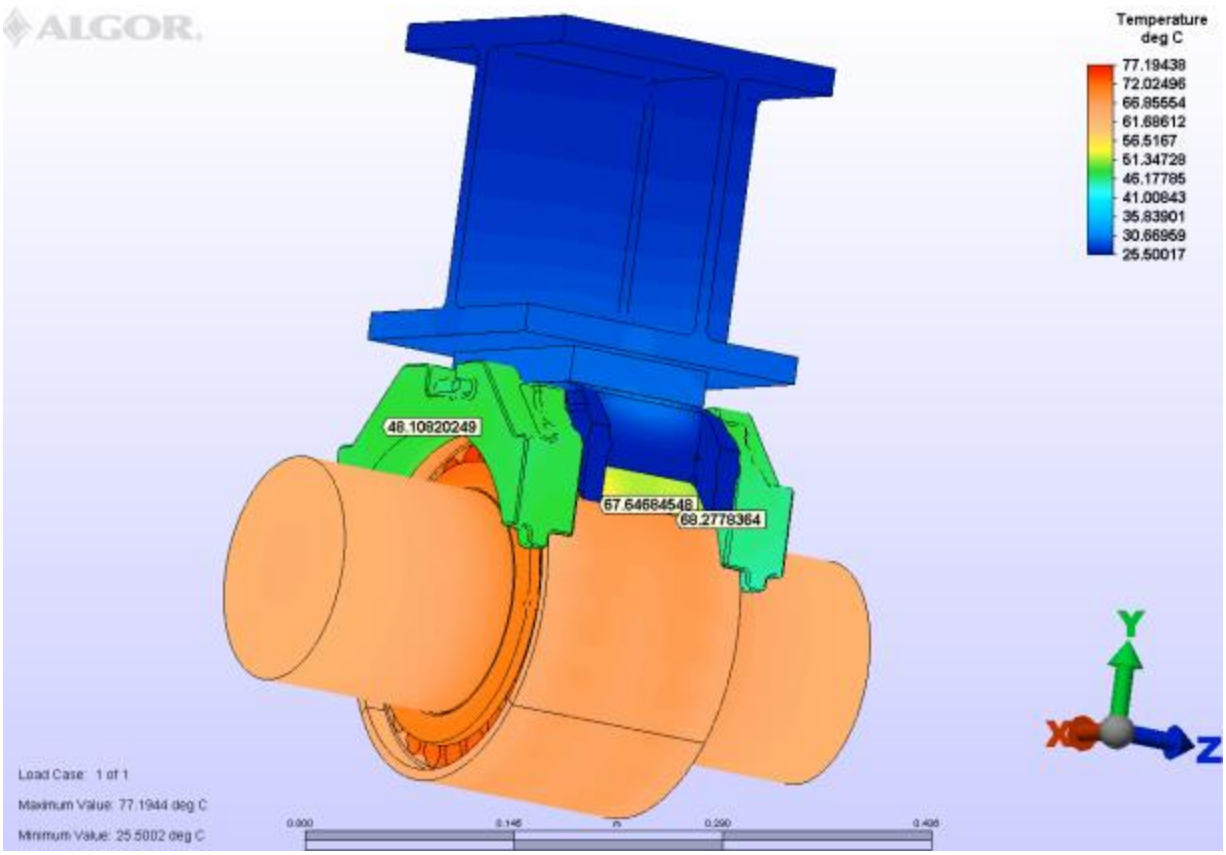

Figure 17: AdapterPlus^{TM} Temperature Distribution – Normal Case [14]

For the sake of completeness, Zagouris [14] also studied the abnormal case for the conventional all-steel adapter to understand its temperature distribution. Figure 18 presents the simulation results for the abnormal bearing operation case study performed on the all-steel adapter.

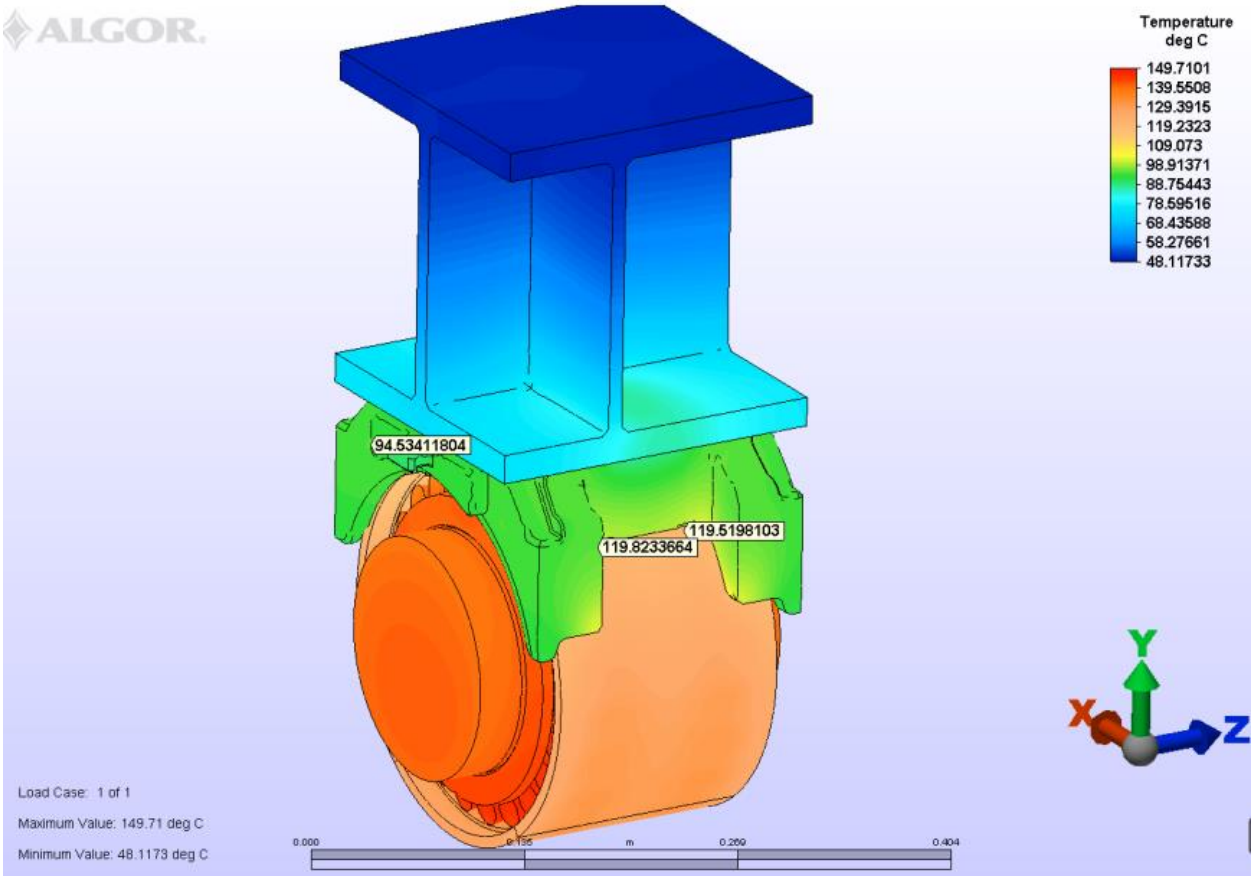

Figure 18: Conventional Adapter Temperature Distribution – Abnormal Case [14]

The proposed models were calibrated and experimentally validated with an IONIX EDGE™ WSN. The downside of the calibration was that it did not account for the tendency of the copper studs to wear with time because of lateral and vertical impact loads and continuous cyclic loading. Note that, once the copper studs lost contact, heat transfer through them was compromised. However, the calibration facilitated the determination of the thermal resistances between the bearing cup (outer ring) and the adapter for both the conventional adapter and the AdapterPlus™. The findings from Zagouris' work helped improve the initial FEM by incorporating two different types of bearing adapters and determining the thermal contact resistances between the bearing and its adapter. Moreover, the adapter temperature distribution

helped calibrate the IONX EDGE™ WSN which was one of the first temperature-based onboard condition monitoring sensors.

Rodriguez [16] utilized the model developed by Zagouris to investigate the effects of the internal heat generation within the polymer suspension pad by observing the thermal behavior of the railroad bearing assembly [14]. Comprehending the effects of the hysteresis heating of the polymer suspension pad during normal and abnormal operating conditions is critical to predict its dynamic response and structural integrity. If the polymer pad structural integrity is compromised, it will lead to uneven loading scenarios to the bearing assembly and will alter the operating conditions. The bearing heat generation is required to obtain the heat distribution within the polymer pad and the adapter itself to observe if the hysteresis heating induced by the polymer pad will affect the overall adapter operating temperature.

The experimental data was obtained by applying different frequencies, low and high, to a transfer molded disk made of the thermoplastic elastomer pad material to observe the effects of internal heating. The results of the testing can be found in Reference [16]. The focus of the study carried out by Rodriguez [ref] was to research the polymer internal heating, which is not germane to this study. However, one important outcome of the work by Rodriguez was the identification of a thermal contact resistance between the bearing adapter and the polymer pad for a fully loaded railcar (100% load), which was found to be 0.01 $m^{2} \cdot K \cdot W^{-1}$ [16]. Since there is no published information on the thermal contact resistance between the adapter and the polymer pad, an optimization study was conducted to match the experimentally acquired data to the numerical results of the FEM, which yielded the value stated earlier.

The findings in the work by Rodriguez demonstrated that the polymer suspension pad did generate heat under cycling loading. However, the heat generated from the polymer pad did not

alter the operating temperatures of the bearing or the adapter. The bearing will have significantly greater heat generation than the polymer pad since the rollers are assumed to be the main heating source and there will be a heat loss through the bearing cup (outer ring) and the adapter. The addition of the thermal contact resistance between the bearing adapter and the polymer pad has a significant impact on the heat transferred between those components. When the bearing operates normally, the polymer pad will not be a liability since elevated temperatures will not be reached at any point in time. Moreover, for the abnormal operation case, the polymer pad may experience elevated temperatures but will not reach the polymer melting temperature of 120ºC (248ºF). If the polymer pad sees a temperature greater than 120ºC (248ºF), its structural integrity will be compromised, which will result in metal-to-metal contact between the adapter and the side frame pedestal roof leading to uneven loading scenarios that can affect the performance of the suspension system.

This literature review served to identify the sources of the boundary conditions used in the proposed finite element model (FEM) of this thesis. The information also provided some insight on the temperature distribution within the bearing components and two different types of bearing adapters under various rail service normal and abnormal operating conditions. However, all the previous models were tested in steady-state conditions and the transient analysis has not yet been studied. The transient analysis will serve to demonstrate whether the bearing adapter can be assumed as a lumped capacitance body and will quantify the thermal time lag between the bearing and the adapter. This information will prove valuable for the proper placement and calibration of onboard wireless sensors affixed to the bearing adapter to monitor the condition of bearings and wheels.

CHAPTER III

LUMPED CAPACITANCE ASSUMPTION VALIDATION

Given the dimensions, geometry, and material composition of the railroad bearing adapter, a question arises as to whether it can be assumed to behave as a lumped capacitance body for the purposes of heat transfer. Hence, heat transfer analytical calculations were performed to determine the Biot number for this engineering application and compare it to the lumped capacitance criterion of Bi < 0.1.

Equation (1) can be used to calculate the Biot number, where U is the overall heat transfer coefficient, L_c is the characteristic length, and k_{adp} is the thermal conductivity of the bearing adapter material, which is cast iron with a value of 38 $W \cdot m^{-1} \cdot K^{-1}$, obtained from the computer-aided design (CAD) software SolidWorks™ material properties library.

$$Bi = \frac{U \cdot Lc}{k_{adp}} \tag{1}$$

Several realistic assumptions were made when carrying out the analytical calculations shown here. First, the adapter was heated by a constant heat flux generated by the frictional heating within the bearing and conducting through the contact surface between the bearing cup (outer ring) and the adapter. Second, the exposed surfaces of the adapter were cooled by forced convection produced by a constant air stream of 5 m/s created by two fans. Third, the ambient temperature used for these calculations was 27°C (81°F).

To obtain the overall heat transfer coefficient, U, Equation (2) was utilized. The calculation requires that the total thermal resistance, R_t, that the adapter experiences must be quantified. The adapter conduction and convection areas must be determined to establish the total area, A_t, where the heat dissipates.

$$U = \frac{1}{R_t \cdot A_t} \tag{2}$$

There are four possible heat transfer paths through the bearing adapter, namely, conduction through the steering polymer pad, conduction through the two copper studs embedded within the polymer pad for electrical conductivity purposes, and convection and radiation through the exposed surfaces of the adapter. Each heat transfer path is associated with its own thermal resistance. Hence, thermal energy generated within the bearing travels through the top of the bearing cup (outer ring) to the bearing adapter and then has four parallel heat transfer paths, each having its own thermal resistance. So, the total equivalent resistance of the four thermal resistances in parallel can be obtained using Equation (3)

$$R_t = \frac{1}{\frac{1}{R_1} + \frac{1}{R_2} + \frac{1}{R_3} + \frac{1}{R_4}} \tag{3}$$

In Equation (3), the convection thermal resistance is denoted as R_1 and is calculated using Equation (4). The adapter has an average convection coefficient, h_{cv}, of 17.9 $W \cdot m^{-2} \cdot K^{-1}$, obtained from reference [14], and a convection surface area, $A_{s,cv}$, of 0.084 m^2 (130.62 in^2). The convection surface area was obtained using the computer-aided design (CAD) software SolidWorks™ by selecting the faces exposed to forced convection. Once the above values were plugged into Equation (4), an R_1 value of 0.665 $K \cdot W^{-1}$ was obtained

$$R_1 = \frac{1}{h_{adp} \cdot A_{s,cv}} \tag{4}$$

Next, the radiation thermal resistance, denoted as R_2 in Equation (3), is calculated using Equation (5), where h_{rd} is the radiation heat transfer cofficient given by Equation (6), and $A_{s,rd}$ is the radiation surface area which is the same as the convection surface area, $A_{s,cv}$, given earlier as 0.084 m^2 (130.62 in^2).

$$R_2 = \frac{L}{k_{pad} \cdot A_s} \tag{5}$$

$$h_{rd} = \varepsilon \cdot \sigma \cdot \left(T_{adp} + T_\infty\right) \cdot \left(T_{adp}^2 + T_\infty^2\right) \tag{6}$$

In Equation (6), ε is the adapter thermal emissivity which is 0.92 as obtained from reference [8], σ is the Stefan Boltzmann constant which is 5.67×10^{-8} $W \cdot m^{-2} \cdot K^{-4}$, T_∞ is the ambient temperature given earlier as 27°C (300 K), and T_{adp} is the adapter surface temperature. For the purpose of these calculations, as a worst-case scenario, the maximum adapter operating temperature of 66°C (339 K), which was reached when the bearing was operating at 137 km/h

(85 mph) under a full railcar load, was used. Plugging the given values into Equation (6) gives a radiation heat transfer coefficient, h_{rd}, of 6.83 $W \cdot m^{-2} \cdot K^{-1}$. Now, inputting the obtained h_{rd} and $A_{s,rd}$ values into Equation (5) gives a radiation thermal resistance, R_2, value of 1.743 $K \cdot W^{-1}$.

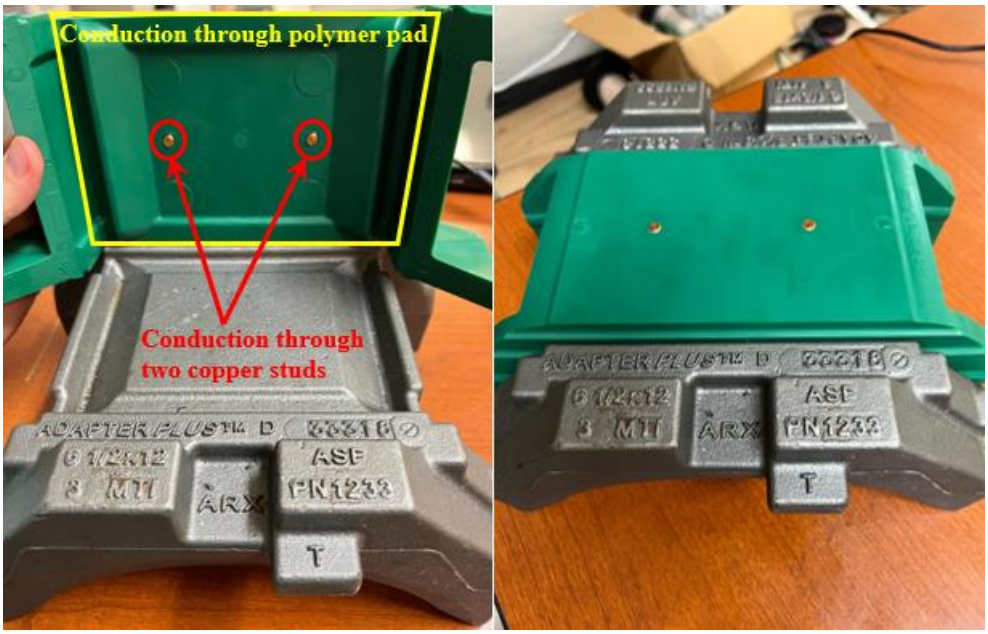

Figure 19: Conduction Paths Through the Adapter Polymer Pad

Figure 19 provides a visual illustration to better understand the conduction heat transfer paths through the adapter. The conduction thermal resistance through the polymer pad is denoted R_3 in Equation (3) and was calculated utilizing Equation (7). In Equation (7), the length, L_p, is the polymer pad thickness since the heat will be transferred from the adapter through the polymer pad thickness. The polymer pad thickness is 0.011 m (0.43 in), and the area of the polymer pad, A_p, through which the heat is transferred is 0.028 m^2 (43.40 in^2). Note that the area of the polymer pad provided excludes the area occupied by both copper pins, depicted in Figure 19. Again, the CAD software SolidWorks™ was used to obtain the exact values of the areas. The thermal conductivity of the polymer pad, k_p, is 0.25 $W \cdot m^{-1} \cdot K^{-1}$ as taken from reference [14]. After plugging the values

into Equation (7), the thermal resistance through the polymer pad, R_3, was found to equal 1.571 $K \cdot W^{-1}$.

$$R_3 = \frac{L_{cp}}{2(k_{cp} \cdot A_{cp})} \tag{7}$$

The final thermal resistance is the conduction heat transfer through the copper pins denoted as R_4 in Equation (3). This thermal resistance was calculated using Equation (8) where the copper pin length, L_{cp}, is equal to the polymer pad thickness of 0.011 m (0.43 in), the copper pin area is 3.43×10^{-5} m^2 and multiplied by two since there are two copper pins present in the polymer pad, and the thermal conductivity of the copper pins, k_{cp}, is 401 $W \cdot m^{-1} \cdot K^{-1}$ as acquired from the property tables of reference [15] at a temperature of 300 K (27°C or 81°F). Inserting the given values into Equation (8) yielded an R_4 value of 0.400 $K \cdot W^{-1}$.

$$R_4 = \frac{L_{cp}}{2(k_{cp} \cdot A_{cp})} \tag{8}$$

Next, the values acquired from Equations (4), (5), (7), and (8) were plugged into Equation (3) to compute the total thermal resistance, R_t. The total thermal resistance value was found to be 0.192 $K \cdot W^{-1}$. The total area, A_t, which includes both the conduction and convection heat transfer surface areas of the adapter was determined to be 0.11 m^2 (170.35 in^2) from the CAD software SolidWorks™. Plugging the calculated values for R_t and A_t into Equation (2), an overall heat transfer coefficient, U, of 47.35 $W \cdot m^{-2} \cdot K^{-1}$ was obtained.

The characteristic length, L_c, of the bearing adapter was calculated by dividing the adapter volume obtained from SolidWorks™ as 1.69×10^{-3} m^3 (102.95 in^3) by the total surface area of 0.11 m^2 (170.35 in^2). The latter gave an adapter characteristic length value of 0.015 m (0.59 in). Finally, the values obtained for the overall heat transfer coefficient, U, adapter characteristic length, L_c, and adapter thermal conductivity, k_{adp}, were plugged into Equation (1) to calculate the Biot number. The calculated Biot number had a value of 0.0191 which is less than 0.1, meaning it satisfies the criterion for a lumped capacitance body. Hence, the above analytical calculations support the assumption that the bearing adapter can be treated as a lumped capacitance body. These calculations were validated by the adapter temperature distribution acquired from laboratory testing and from the finite element model (FEM) simulations performed for this study.

CHAPTER IV

LABORATORY AND FINITE ELEMENT MODEL SETUP

4.1 Four Bearing Chamber Tester (4BCT)

The University Transportation Center for Railway Safety (UTCRS) dynamic test rig housed at the University of Texas Rio Grande Valley (UTRGV) was used to conduct the laboratory testing for this study. The objectives of the conducted experimental testing were as follows: (1) verify that the bearing adapter acts as a lumped capacitance body, (2) find the appropriate thermal contact resistance between the bearing adapter and the thermoplastic polyurethane (TPU) pad for a fully loaded railcar and an empty railcar, (3) validate the reliability and efficacy of the developed finite element model (FEM) in simulating the transient heat transfer behavior of the railroad bearing and adapter resulting from changes in operating conditions, and (4) quantify the thermal time constants for the bearing adapter in response to changes in operating conditions.

The dynamic bearing test rigs are designed to simulate the operating conditions experienced by railroad tapered roller bearings in rail service. The laboratory experiments were mainly performed in the four-bearing chamber tester (4BCT), depicted in Figure 20. This tester can run four distinct classes of railroad bearings, namely: Class E (6"×11 "), Class F (6½"×12 "), Class G (7"×12 "), and Class K (6½"×9 ") tapered-roller bearings. According to the Association of American Railroads (AAR) standards, full load on a class K or F railcar bearing is rated at 153

kN (34.4 kips) per bearing. The 4BCT is equipped with a hydraulic cylinder that can apply vertical loads up to 150% of the full railcar load.

The experimental data presented in this thesis were acquired at two bearing loading conditions: 153 kN (34.4kips) per bearing which corresponds to a fully loaded railcar (100% load), and 17% of full (i.e., 26 kN or 5.85 kips per bearing) load which emulates an empty railcar. To maintain the load constant at either the 100% or 17% setting, an external load controller is utilized. The external load controller is powered by a DC motor that transforms rotational energy into translational energy with the aid of a threaded rod and a gearbox. The DC motor is regulated by a LabVIEW^{TM}-based circuit, which sends a signal and regulates the applied load within ±1,560 N (350lb) of the targeted loading scenario.

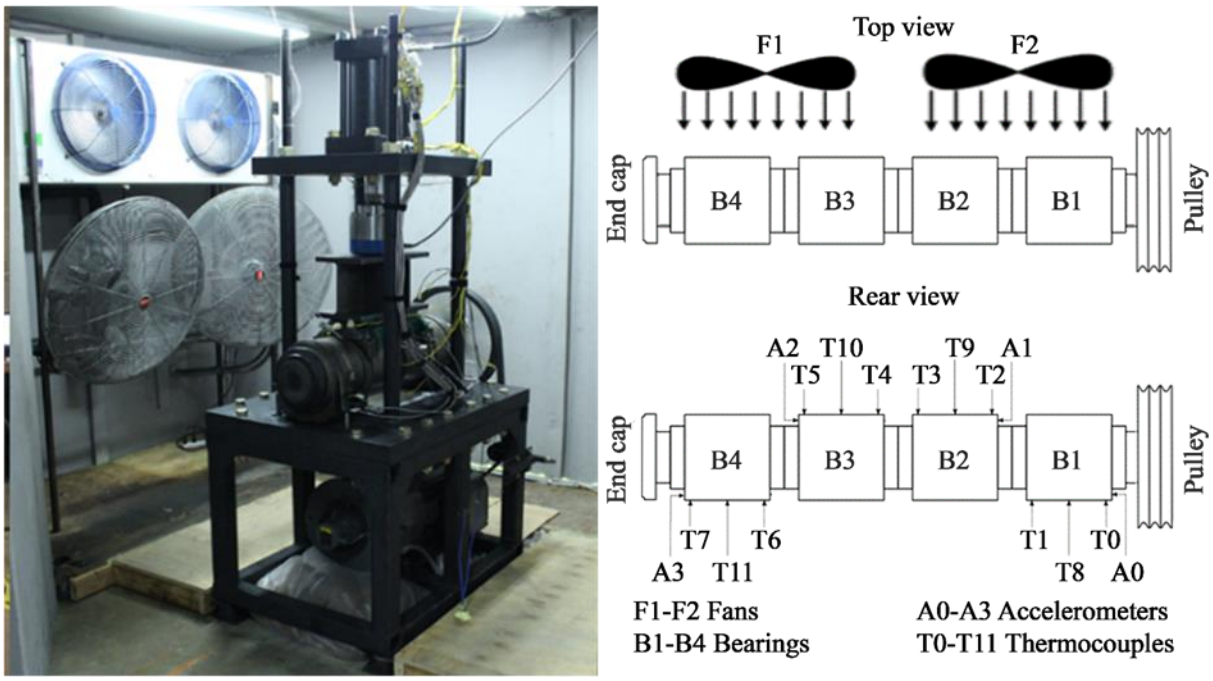

Figure 20: Four Bearing Chamber Tester (4BCT) Picture (Left) and Instrumentation Schematic (Right)

The 4BCT is equipped with a 22 kW (30 hp) variable speed motor which allows the bearings to be tested at different simulated train traveling speeds, shown in Table 2. The motor is controlled with a variable frequency driver (VFD) which will accurately maintain the chosen angular speeds within 0.5%. The motor power data is collected from the VFD every twenty seconds and is later used to calculate the average motor power to obtain the roller heat flux. As depicted in Figure 20, there are two industrial fans that provide convection cooling to the test bearings through an air stream with an average velocity of 5 m/s (11.2 mph). Additionally, tone of the main features of the 4BCT is that it can provide controllable ambient temperatures ranging from -40 to 65ºC (-40 to 150ºF).

Table 2: Common Simulated Train Speeds Used in this Study

Axle Speed [rpm]	Track Speed [km/h]	Track Speed [mph]
234	40	25
327	56	35
420	72	45
514	89	55
618	106	66
796	137	85

The configuration of the bearings on the test axle is illustrated in the instrumentation schematic provided in Figure 20. The two middle bearing positions (B2 and B3) are top-loaded mimicking rail service conditions, while the two-end bearings (B1 and B4) are bottom-loaded and serve as control (defect-free) bearings. The bearing adapters for both top-loaded bearings are instrumented to collect the vibration and temperature data during the laboratory testing. For this study, only the acquired temperature data id of interest and, therefore, the vibration data and instrumentation will not be discussed.

Figure 21 shows the locations of the temperature sensors used to track and record the temperature histories of both the bearing and its adapter. For the bearing, two spring-loaded bayonet-style K-type thermocouples along with a single K-type thermocouple that is held tightly against the outside surface of the bearing cup (outer ring) at the spacer ring location via a hose clamp were used, as picture in Figure 21 (Right). The mean value of these three thermocouples represents the bearing operating temperature, which will be directly compared to the results

obtained from the FEM simulations. For the adapter, the location of the single K-type thermocouple used to monitor and record the adapter operating temperature is shown in Figure 21 (Left). A set screw is used to push down on the thermocouple end to secure it in place in the specially drilled hole. To avoid any air interference with the temperature readings of the bearing adapter K-type thermocouple, a sealant was used to isolate the thermocouple. The sealant used is ASTM C920 Class 35, which stands for Elastomeric Joint Sealants that can be cured at low temperatures. This sealant is commonly used to safeguard against leaks in doors and windows. The sealant was applied around the thermocouple and left to cure. After curing, a simple test was performed to check if there was any air interference. This involved monitoring the adapter thermocouple readings before and after the fans were turned on and making sure that the readings were stable and did not fluctuate significantly after the fans were on. The temperature readings acquired from the thermocouple affixed to the bearing adapter were later compared to the results of the FEM simulations.

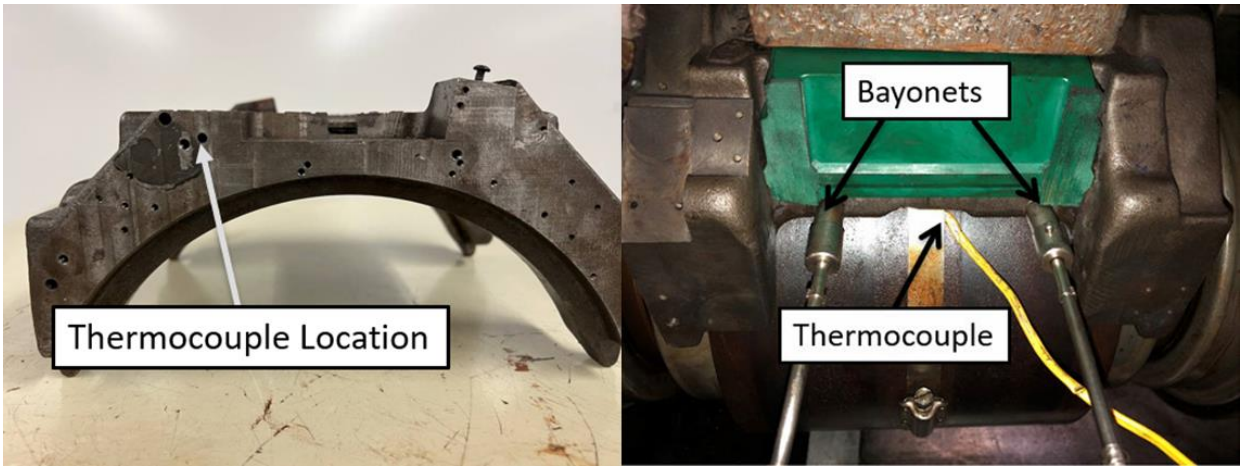

Figure 21: Temperature Sensor Locations for the Adapter (Left) and the Bearing (Right)

4.1.2 LabVIEW™ Based Load Controller

Data acquired from a 445 kN (100 kip) Interface® load cell is transmitted to a computer running LabVIEW™ every twenty seconds interval via a National Instruments (NI) USB-6008 data acquisition (DAQ) system. An error loop in the program adjusts the applied load based on the given values of the load cell every two minutes. If the load cell error exceeds the tolerance of ±1,560 N (350lb), a NI USB-6211 sends a five-volt pulse signal via the digital output port to the load motor controller to adjust the load until the applied load is within the specified tolerance.

4.2 Data Acquisition System

A NI cDAQ-9174 DAQ programmed using LabVIEW™ was used to record and collect all the experimental data for this study. A NI 9213 card was used to collect the K-type thermocouple temperature data with a sampling frequency of 128 Hz for half a second, in intervals of twenty seconds. The acquired data is later processed utilizing scripts available through the mathematical software MATLAB®, and plotted for visual representation purposes.

4.3 Finite Element Model

An experimentally validated transient thermal finite element model (FEM) that was developed to obtain temperature distributions maps of complete bearing assemblies in operation is presented hereafter. A computer aided design (CAD) model was created in SolidWorks™ to develop FEM. The FEM consists of a class F bearing press-fit onto an axle and equipped with an AdapterPlus™ that supports a steel spacer plate and an I-beam that mimic the functionality of the side frame. In detail the model components are: two bearing cone (inner ring) assemblies press-fit onto the axle and separated by a steel spacer ring, a bearing cup (outer ring), bearing adapter fitted with a thermoplastic elastomer pad, a steel spacer plate, and a steel I-beam, as illustrated by the mesh diagram of Figure 22. A total of 146,202 mesh elements were used to generate the FEM depicted in Figure 22. A combination of brick, pyramid, tetrahedral, and wedge elements were used to successfully mesh the aforementioned model. In the FEM, it is assumed that all 46 rollers (23 rollers per cone assembly) generate equivalent amounts of heat rate in the system. The length of the axle accounts for the different thermal runways partially caused by the insulating properties of the thermoplastic elastomer suspension pad at the other end of the system and considers the heat dissipation from the neighboring bearings on the complete test axle.

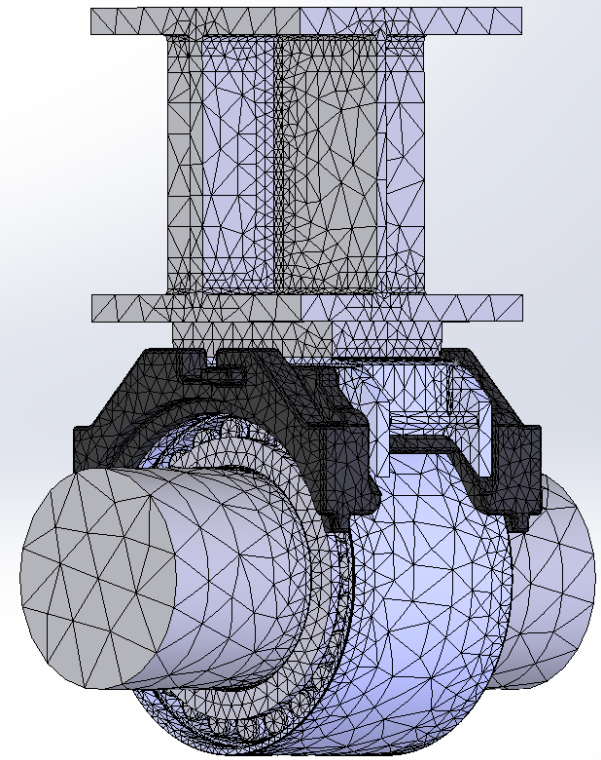

Figure 22: FEM Mesh of a Class F Bearing Press-Fit onto an Axle and Fitted with an AdapterPlus^{TM} that supports a Steel Spacer Plate and an I-Beam

Some boundary conditions and overall heat transfer coefficients were acquired from previous theorical and experimental work [12]. Five major boundary conditions were applied: convection, conduction, radiation, heat generation, and heat flux. The model's complexity was lessened by neglecting the presence of bearing cone polymer cages, seals, wear rings, and grease. The thermal resistances of both the grease and the polyamide cage are substantial compared to the other bearing components, and their omission is justified in Reference [14]. Since this is a static model, the actual rotation of the cone assembly inside the bearing was not directly simulated but was instead considered by applying an average heat flux through all 46 rollers inside the bearing. It was also assumed that the total input motor power was distributed evenly

across the four bearings of the 4BCT, which was justified given that the operating temperatures of all four bearings on the test axle were within ±2°C.

To obtain the average input motor power, the data is plotted using the mathematical software MATLAB®, and built-in functions within the software package are utilized to obtain the average value for a selected region within the plot. Figure 23 serves as an example of a region that was selected (region between dashed lines) to obtain the raw data of the input motor power and then compute the average motor power. Since only one bearing was simulated, the average input motor power was first divided by four and then converted into the individual roller heat flux by dividing it by 46, the total number of rollers within a bearing, and then by the roller circumferential surface area which is roughly equal to 33.61 cm^2 (5.21 in^2).

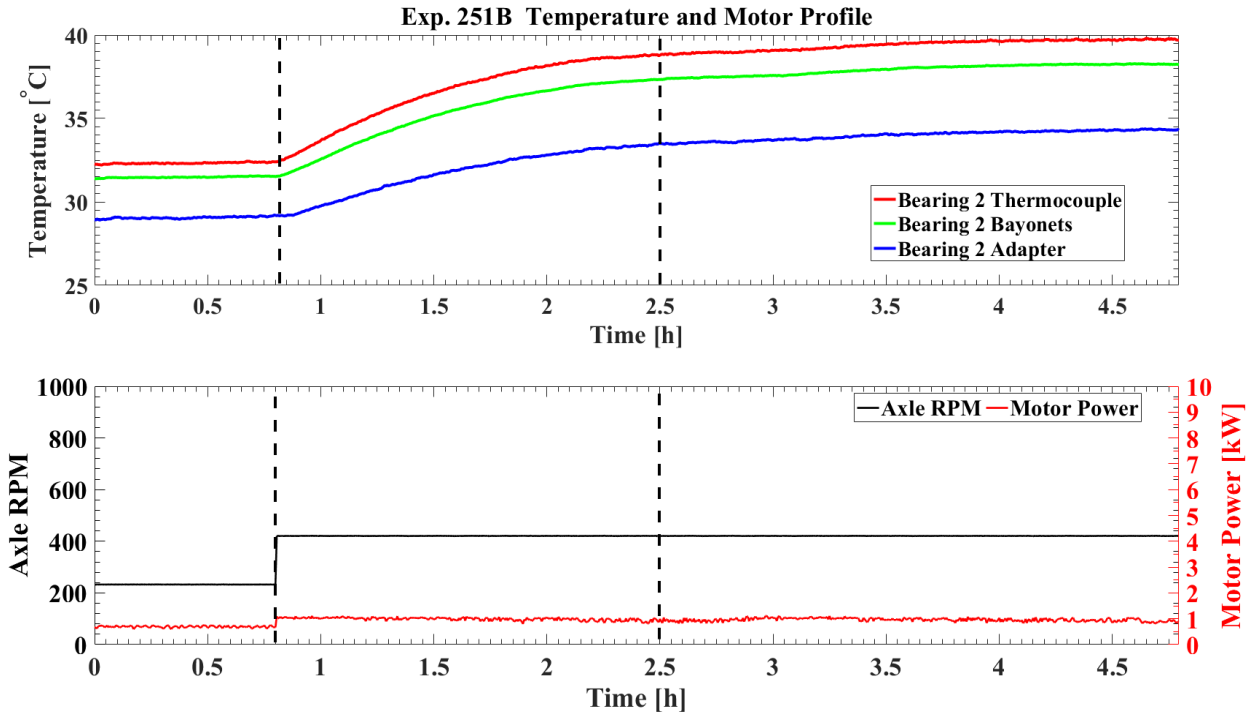

Figure 23: Experiment 251B Bearing 2 Experimental Data

Material properties for the bearing components, adapter, axle, I-beam, and spacer plate were all directly selected from SolidWorks™. AISI 1035 Steel with thermal conductivity of 52 $W \cdot m^{-1} \cdot K^{-1}$ was used for axle, I-beam, and spacer plate. AISI 4340 Steel with a thermal conductivity of 44.5 $W \cdot m^{-1} \cdot K^{-1}$ was selected for the bearing components. The properties of the bearing adapter polymer pad material were sourced from BASF literature for thermoplastic polyurethane (TPU) considering grades with the same Shore durometer value. Cast alloy steel was selected for the bearing adapter material with a thermal conductivity of 38 $W \cdot m^{-1} \cdot K^{-1}$. Average convection coefficients values for the FEM components are listed in Table 3. These values obtained from previous related work [12] [14][16].

Table 3: Convection Coefficients Used for this Study

Component	$\bar{h}$ [W·m^{-2}·K^{-1}]
Axle	25.0
I-beam	19.0
Spacer Plate	18.3
AdapterPlus^{TM}	17.9
AdapterPlus^{TM} Pad	17.9

The convection and radiation boundary conditions for the bearing cup was acquired from previous theorical and experimental work summarized in References [8], [11], and [14]. For the exposed surface area of the bearing cup, an overall heat transfer coefficient of H_o = 8.32 W·K^{-1} was applied, which represents forced convection generated by 5 m/s cross-flow of air over the bearing and radiation heat transfer to ambient air at a temperature of 25ºC (77ºF). To satisfy the required software units, the overall heat transfer coefficient must be divided by the cup surface area, which is roughly 0.1426 m^2 (221 in^2), resulting in a cup overall heat transfer coefficient of h_o = 58.4 W·m^{-2}·K^{-1}. The axle heat transfer convection coefficient was obtained by utilizing the Nusselt number correlation for a cylinder in cross flow [15]. Zagouris et.al [14], calculated the average convection heat transfer coefficient of the axle to be $\bar{h}_{axle}$ = 25 W·m^{-2}·K^{-1}. The average convection heat transfer coefficients, listed in Table 3, for the bearing adapter, adapter pad, I-beam, and spacer plate, were also computed using the Nusselt number correlations for a flat plate in parallel flow [14]. The convection, radiation and heat flux boundary conditions were applied to the FEM as illustrated in Figure 24. The regions in green color had convection only, the

regions in orange had convection and radiation, and the regions in red denote the applied roller heat flux.

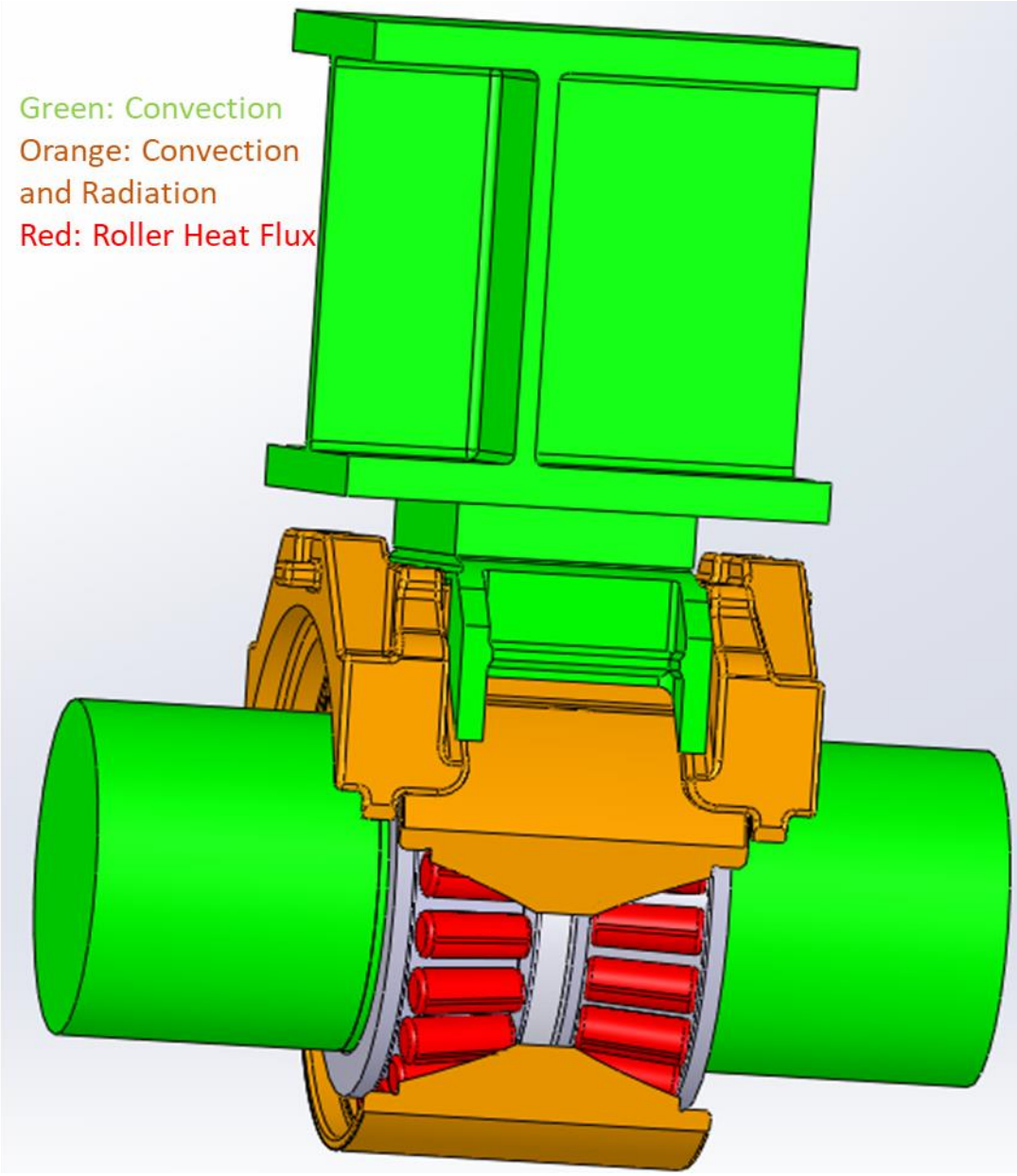

Figure 24: FEM with Applied Boundary Conditions

Thermal contact resistance between the bearing adapter and the bearing cup (outer ring) contact surfaces affects the amount of heat transferred from the bearing to the adapter. The

thermal contact resistance varies depending on several factors which include the loading conditions of the freight car whether it is empty or fully loaded, the type of bearing adapter that is being used, and the condition of the contact surfaces. For instance, new bearings and adapters will have clean smooth surfaces (ideal conditions) which enhances the contact between them and reduces the thermal contact resistance. On the contrary, surfaces of bearings and adapters in rail service will have some roughness to them due to several factors such as accumulated rust from environmental conditions, wear, and more, which can increase the thermal contact resistance.

Based on a previous study conducted by Zagouris [14] who used pressure film to quantify the contact pressure between the bearing cup (outer ring) and the adapter, a thermal contact resistance value of 0.0055 $m^{2} \cdot K \cdot W^{-1}$ was applied between the bearing cup and the adapter. An additional thermal contact resistance was applied between the bearing adapter and the polymer pad. This thermal contact resistance values differs between a fully loaded railcar (100% load) and an empty railcar (17 % load) since the contact pressure between the polymer pad and the metal adapter is five times higher in the case of a fully loaded railcar. Since there is no information in the literature regarding the thermal contact resistance between the metal adapter and the polymer pad, an optimization study was performed to determine the values at both fully loaded and empty railcar operating conditions. The optimization study involved the systematic comparison of the steady state bearing adapter operating temperature acquired from laboratory testing with the corresponding FEM simulations at both loading scenarios. Based on the optimization results, the thermal contact resistance value for a fully loaded railcar (100% load) was determined to be around 0.01 $m^{2} \cdot K \cdot W^{-1}$ while the value for an empty railcar (17% load) was about 0.02 $m^{2} \cdot K \cdot W^{-1}$.

4.3.1 FEM Simulation Setup

Since this is a transient thermal analysis, some parameters must be defined before running the simulations. For example, the time step and the simulation time required to run the analysis. Other factors to take into consideration are the initial temperatures for each component of the assembly. These temperatures were obtained from a steady-state analyses that were run with the average input motor power at 40 km/h (25 mph) for both a fully loaded railcar (100% load) and an empty railcar (17% load) operating conditions. For illustrating purposes, Figure 25 displays the total simulation time of 30,865 seconds with a time step of 600 seconds for the simulated operating scenario of an empty railcar traveling at a speed of 106 km/h (66 mph).

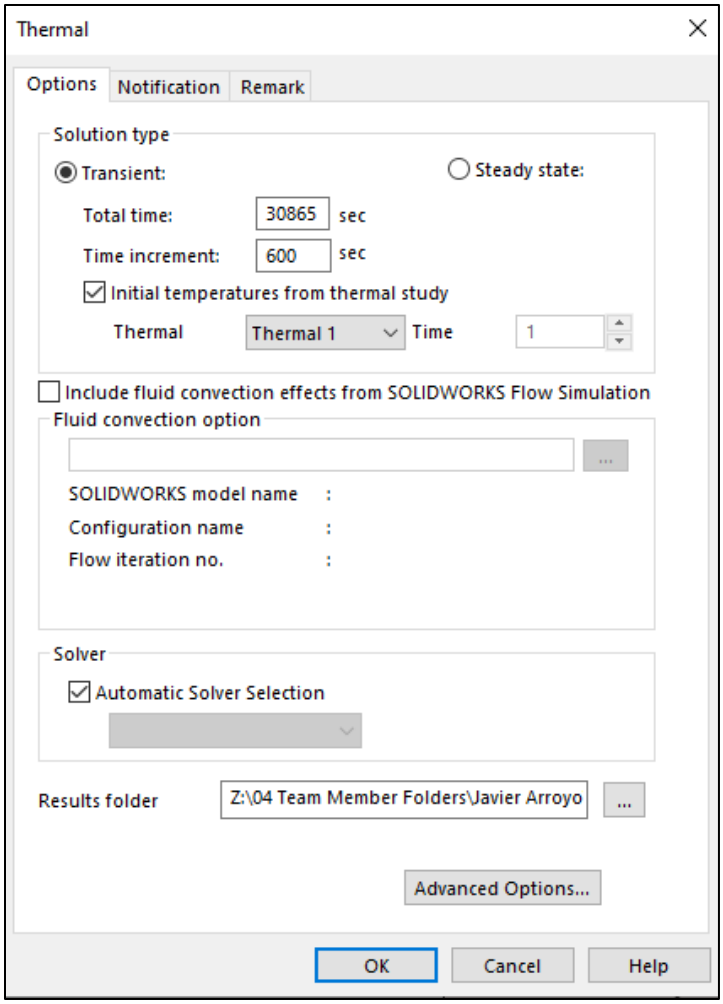

Figure 25: FEM Time Parameters Setup Display

Once the steady-state simulation concluded, the temperature values were obtained through selected node locations with the aid of the probe feature in SolidWorks™. The FEM temperature nodes were chosen based on the experimental temperature sensor setup pictured in Figure 21. That is, the three FEM temperature nodes chosen corresponded to the three temperatures acquired experimentally from the two bayonet-style K-type thermocouples that monitored the temperature of each cup raceway, and the regular K-type thermocouple that tracked the temperature at the middle of the bearing cup. Hence, the average bearing operating temperature from the simulations was obtained by averaging the temperatures of the three chosen

FEM nodes. Similarly, the average bearing operating temperature from the laboratory testing was acquired by calculating the mean of the three thermocouple readings. For the bearing adapter, the FEM temperature node chosen corresponded to the exact location of the actual K-type thermocouple affixed to the adapter. The efficacy and reliability of the FEM was assessed through direct comparison of the simulated and actual operating temperatures of the bearing adapter. Figure 26 provides a visual representation of the location of each FEM node chosen for the bearing and the adapter along with their respective temperature values.

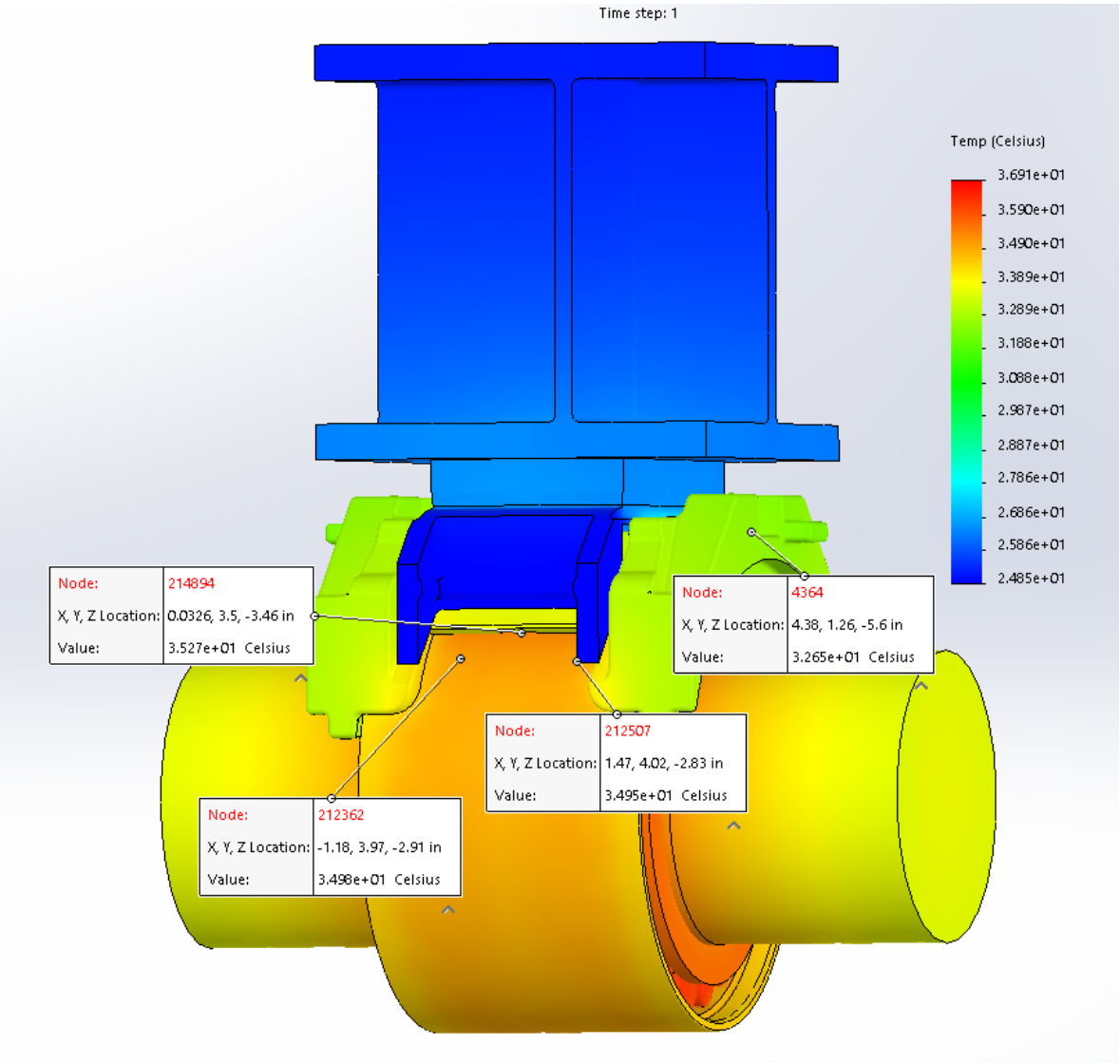

Figure 26: FEM Node Selection with Temperature Results

After getting the steady-state temperature values for the simulated operating scenarios of an empty and fully loaded railcar traveling at 40 km/h (25 mph), they were utilized as initial temperatures for the transient FEM simulation. As mentioned earlier, the total simulation time and the time step values were first defined. For this study a time step of 600 seconds (10 minutes) was selected based on a performed convergence analysis which revealed that the simulation temperatures at the 10-minute mark obtained utilizing a 30-second time step versus a

600-second time step were will within 0.1°C difference, as demonstrated by Table 4 and Table 5 for the bearing and the adapter, respectively. Hence, the choice of the 600-second (10 minute) time step used in the FEM simulations performed for this study was justified.

Table 4. Convergence Analysis for the Bearing Operating Temperature

Bearing			
First 10 minutes of temperature data			
Time [sec]	Actual Temperature [ºC]	FEM Simulation (30 sec) [ºC]	FEM Simulation (10 min) [ºC]
30	32.62	35.07	
60	32.65	35.10	
90	32.66	35.12	
120	32.69	35.14	
150	32.69	35.17	
180	32.70	35.19	
210	32.71	35.21	
240	32.74	35.23	
270	32.77	35.24	
300	32.76	35.26	
330	32.81	35.27	
360	32.80	35.29	
390	32.82	35.30	
420	32.84	35.32	
450	32.87	35.33	
480	32.86	35.35	
510	32.89	35.36	
540	32.91	35.37	
570	32.92	35.38	
600	32.92	35.39	35.36

Table 5. Convergence Analysis for the Bearing Adapter Operating Temperature

Adapter			
First 10 minutes of temperature data			
Time [sec]	Actual Temperature [ºC]	FEM Simulation (30 sec) [ºC]	FEM Simulation (10 min) [ºC]
30	29.66	31.65	
60	29.62	31.65	
90	29.64	31.65	
120	29.66	31.65	
150	29.67	31.65	
180	29.72	31.66	
210	29.72	31.66	
240	29.76	31.66	
270	29.73	31.66	
300	29.72	31.67	
330	29.76	31.67	
360	29.73	31.67	
390	29.76	31.68	
420	29.79	31.68	
450	29.82	31.69	
480	29.86	31.69	
510	29.87	31.7	
540	29.90	31.7	
570	29.93	31.71	
600	29.92	31.71	31.73

The total simulation time depends on the time needed to reach steady-state operating conditions. Meaning, if the 4BCT is set to 40 km/h (25 mph) under an empty railcar load and after reaching steady-state operating conditions, the speed was changed to 72 km/h (45 mph), then the time required to reach steady-state conditions will be less than that needed if the speed were changed to 137 km/h (85 mph) instead. Therefore, each speed variation will require a different simulation time depending on how long it takes the bearing and the adapter to reach steady-state operating conditions.

CHAPTER V

RESULTS AND DISCUSSION

Once the parameters and boundary conditions for the finite element model (FEM) were defined, numerical simulations were run and the results were compared to the experimentally acquired date for validation purposes. The laboratory testing phase consisted of running two reconditioned bearings in the B2 and B3 locations and two control bearings in the B1 and B4 locations (refer to Figure 25), under two loading conditions and several speed variations. Test Bearing 2 (B2) was selected to obtain the average operating temperatures of the bearing and the adapter since it experienced normal operating conditions. In contrast, Test Bearing 3 (B3) exhibited some abnormal operating behaviors, such as temperature fluctuations throughout the experimental testing, which required longer simulation times to achieve the steady-state operating conditions.

There were a total of ten case scenarios investigated in this study, which will be thoroughly discussed in this Chapter. For each loading scenario, fully loaded railcar (100% load) and empty railcar (17% load), a total of five speed variations were executed experimentally utilizing the four bearing test rig and simulated using the developed finite element model. The speed variations were as follows: 40 to 56 km/h (25 to 35 mph), 40 to 72 km/h (25 to 45 mph), 40 to 89 km/h (25 to 55 mph), 40 to 106 km/h (25 to 66 mph), and 40 to 137 km/h (25 to 85 mph). The first five cases were run at an empty railcar load condition (17% load) condition.

In each case, the tester speed was set at 40 km/h (25 mph) at the desired load condition and allowed to reach steady-state operating conditions before the tester speed was increased to 56 km/h in Case 1, 72 km/h in Case 2, 89 km/h in Case 3, 106 km/h in Case 4, and 137 km/h in Case 5. The average ambient temperatures for Case 1 through Case 5 for the empty railcar scenario were 24ºC (75ºF), 24ºC (75ºF), 26ºC (79ºF), 26ºC (79ºF), and 27ºC (81ºF), respectively. The ambient temperatures were defined and inputted into the FEM parameters, since the model requires an ambient bulk temperature.

Since freight trains run either fully loaded or empty, the only way to affect change in the heat generation rate within a healthy (defect-free) bearing is by increasing the operational speed. Hence, Case 1 through Case 4 are attempts to mimic realistic rail service operating conditions where the train speed might be increased once the train leaves an urban area. Case 5 is not common at all in freight rail service but is meant to provide a worst-case scenario for the heat generation within a bearing to simulate situations where a bearing might be developing a defect or operating abnormally.

The remaining five cases, Case 6 through Case 10 were like Case 1 through Case 5 but were run at the fully loaded railcar scenario (100% load). The average ambient temperatures for Case 6 through Case 10 were 28ºC (82ºF), 26ºC (79ºF), 26ºC (79ºF), 27ºC (81ºF), and 29ºC (84ºF). After running the numerical situations, the resulting data was organized and compared to the results acquired from the laboratory testing performed on the four-bearing test rig.

5.1 Bearing and Adapter Operating Temperature Results

Experiment 251B featured two reconditioned bearings undergoing service life performance testing which included running the bearings at different load and speed operating conditions. As previously discussed, the reconditioned bearings were placed in the B2 and B3 bearing locations with bearing B2 being selected to validate the proposed transient FEM in this thesis. The operating temperature and input motor power profiles for test bearing 2 (B2) are presented in Figure 27.

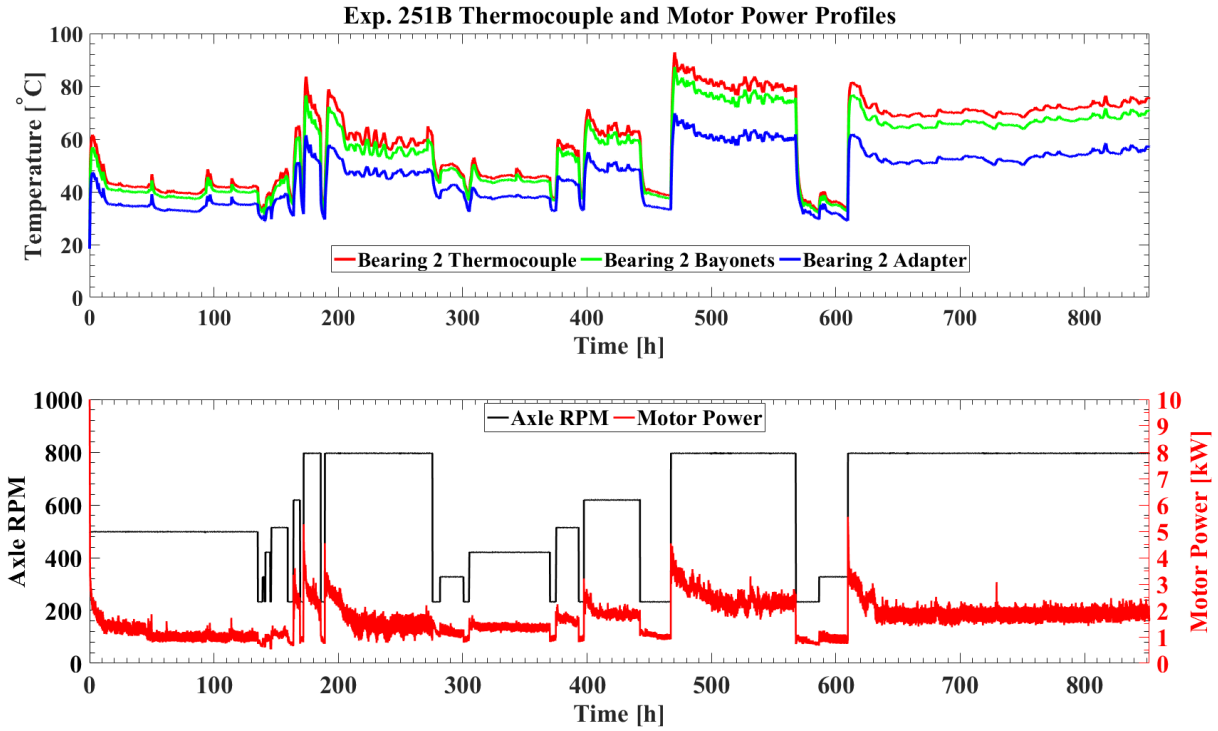

Figure 27: Temperature and Motor Power Profiles for Experiment 251B

For the first 150 hours of this experiment, the bearings ran at 85 km/h (53 mph) under an empty railcar load (17% load) to allow the grease to break in. Once this stage was cleared, the aforementioned ten case scenarios were executed. The initial speed was set to be 40 km/h (25 mph), and then the speed was increased depending on the specific case scenario being studied.

For example, after the break in period ended, the four-bearing chamber tester (4BCT) was set to a simulated train speed of 40 km/h under an empty railcar load and allowed to reach steady state operation. Then the tester speed was increased to 56 km/h for Case 1 and allowed to achieve steady-state operating conditions so the temperature data could be tracked and recorded. Following that, the tester speed was decreased back to the initial speed of 40 km/h and allowed to reach state-state operation before the speed was increased to 72 km/h for Case 2. This process was repeated until all five cases for the unloaded (empty) railcar scenario were done. The unloaded railcar experiments were conducted first because the bearing requires less time to reach steady-state operating conditions compared to the fully loaded railcar scenario. The calculated average motor power per speed variation is presented in the Appendix. Note that each case scenario studied will have its unique motor power and roller heat flux, which is expected given the roller-raceway dynamics and that the grease viscosity is highly dependent on the bearing operating temperature. Visual comparisons of the transient temperature data acquired experimentally and through the FEM simulations for both the bearing and the adapter under an empty railcar load (17% load) are presented in Figure 28 and Figure 29, respectively.

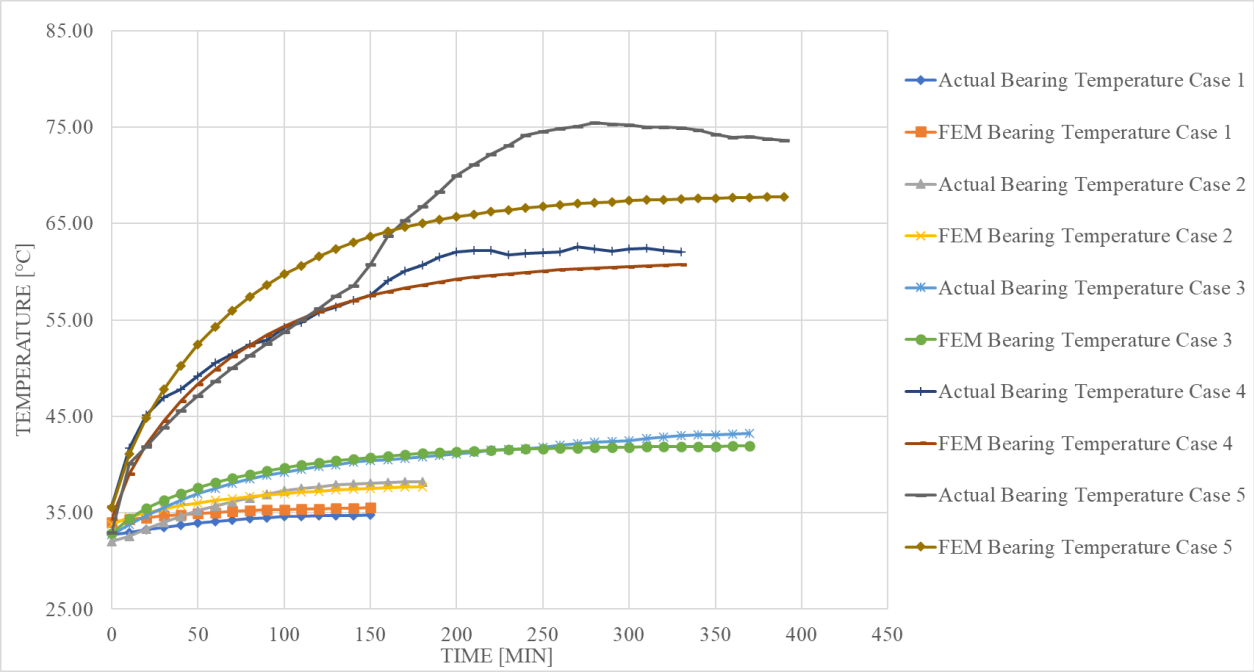

Figure 28: Bearing Operating Temperature Master Plot at Empty Railcar Conditions

Figure 28 displays all five cases for the empty railcar (17% load) scenario. The data acquired for all five cases, which was used to generate Figure 28, can be found in the Appendix, along with the respective FEM-results-to-experimental-data percent errors and the specific roller heat flux used in each case. From Figure 28, it can be observed that the bearing experiences normal operating conditions for Case 1 through Case 4 with a maximum temperature difference between the FEM results and the laboratory data of 2°C (~4°F). On the other hand, at higher speed variation of Case 5, the bearing exhibits some abnormal behavior most likely due to roller misalignments, and the FEM is not able to recreate this abnormal trend. As explained earlier in this thesis, one of the limitations of the proposed FEM is that a transient motor power cannot be inputted into the software parameters and, therefore, the FEM cannot mimic the abnormal temperature profile experienced by the actual bearing. Despite this limitation, and recalling that Case 5 is a worst-case scenario, the steady-state operating temperatures acquired from the FEM

and the laboratory testing are within 6°C (~11°F) when compared to one another. The results provided in Figure 28 validate the developed FEM as a reliable tool in predicting the transient and steady state bearing operating temperature at empty railcar conditions (17% load).

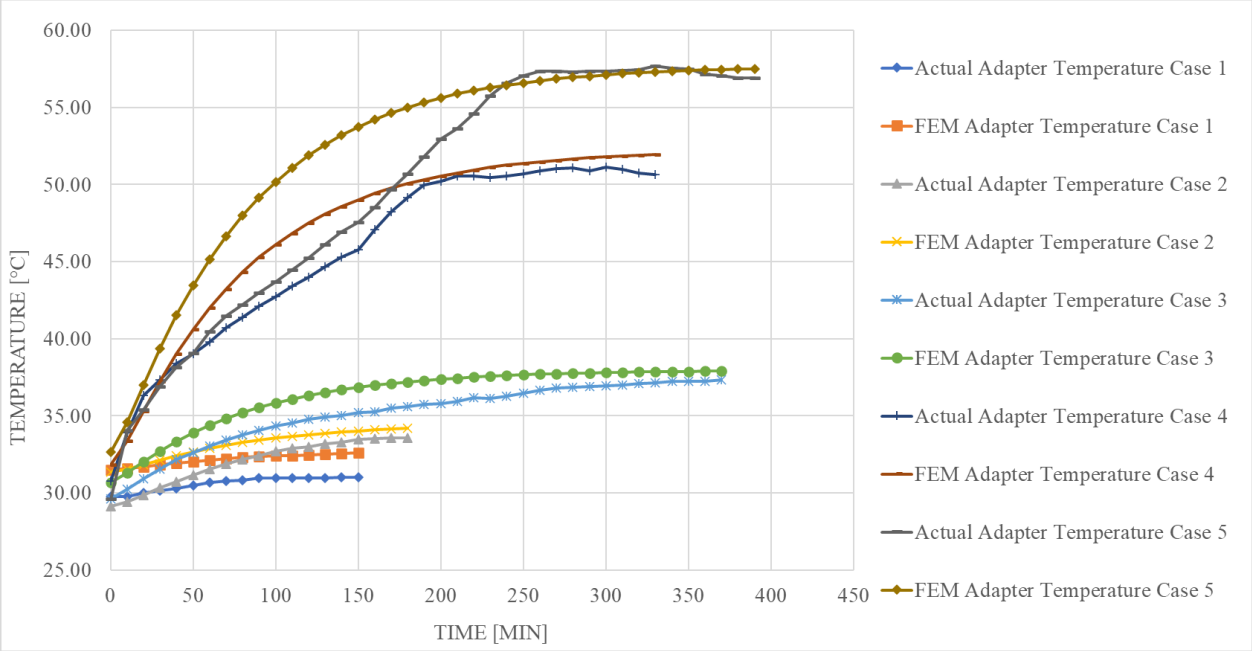

Figure 29: Adapter Operating Temperature Master Plot at Empty Railcar Conditions

Figure 29 is a plot of the adapter temperature data acquired from the FEM simulations and the experimental testing for all five cases studied for the empty railcar (17% load) scenario. The complete data set can be found in the Appendix along with the respective percent error from the comparison between the FEM simulation temperatures and the experimentally acquired temperatures. As expected, for all five cases studied, the adapter operating temperature followed similar trends as those of the bearing operating temperature since the bearing serves as the heat generation source. In general, for the three lowest speed variations (i.e., Case 1 through Case 3), the bearing operated normally and, therefore, the experimental data and the FEM simulation results for the bearing adapter were within 1-2°C (~2-4°F) throughout the transient response

leading to the steady-state operation. For Case 4 and Case 5, which involved higher speed variations, the bearing was more susceptible to roller misalignments, especially at the empty railcar load, that resulted in temperature differences of 3-6°C (~5-11°F) during the transient response time. However, the steady state operating temperatures for the bearing adapter acquired numerically and experimentally were all within 1-2°C (~2-4°F), which demonstrates the validity of the developed FEM in predicting the transient and steady state adapter operating temperatures in response to normal increases in heat generation rates within the bearing.

Moreover, by comparing Figure 28 and Figure 29, one can notice a slight time lag between temperature events occurring at the bearing and adapter, respectively. For example, looking at the transient response of Case 4, the bearing operating temperature seems to have reached steady-state operation at about the 200-min mark, whereas the corresponding event on the adapter operating temperature profile occurs about 10 minutes later around the 210-min mark. This 10-min thermal time lag between the bearing and the adapter is in line with the time constant data presented at the end of this chapter.

After Case 5 concluded, the tester speed was decreased to 40 km/h and the load was increased to simulate a fully loaded railcar (100% load). Once steady state operation was reached, the next five case scenarios (i.e., Case 6 through Case 10) were run in a similar fashion to what was done for Case 1 through Case 5 but for the fully loaded railcar scenario. The corresponding bearing and adapter operating temperatures are presented in Figure 30 and Figure 31, respectively, for all five cases studied. The data sets acquired numerically and experimentally can be found in the Appendix along with the respective percent errors from the comparison between the FEM simulation temperatures and the laboratory testing temperatures.

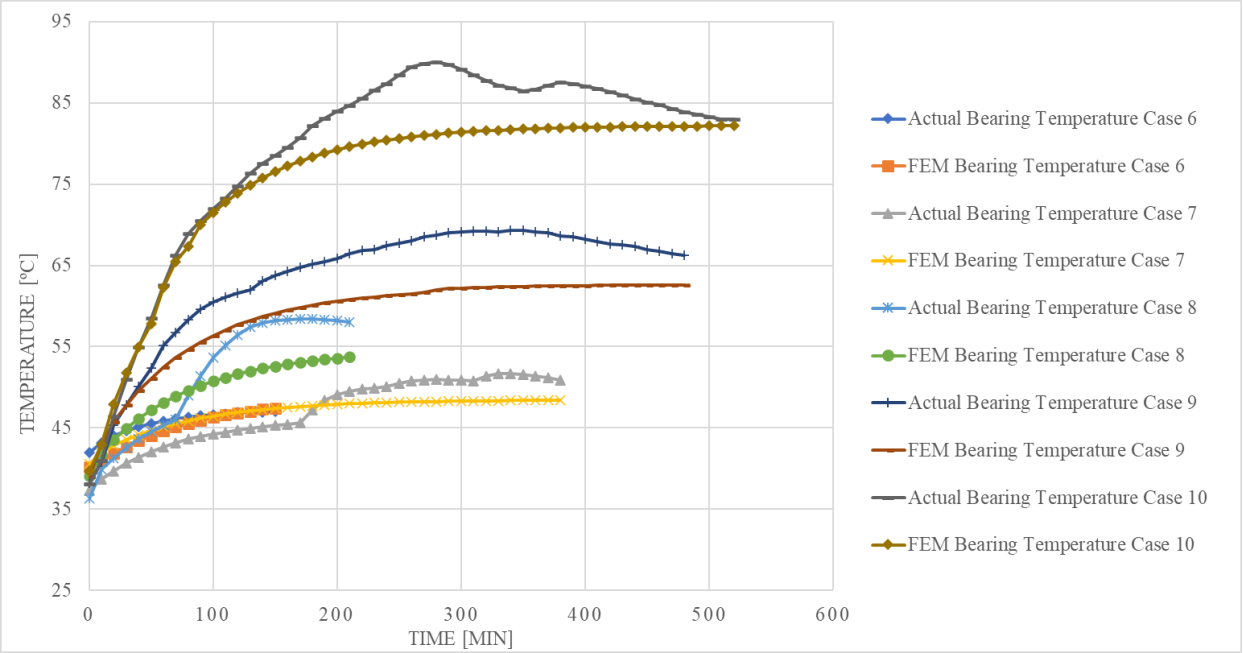

Figure 30: Bearing Operating Temperature Master Plot at Fully Loaded Railcar Scenario

Looking at Figure 30, it can be noticed that, except for Case 6 where the speed was increased from 40 to 56 km/h, the bearing heating was associated with some abnormal behavior at some point during the transition from one speed to the other. Case 7 through Case 10 serve as an example of how roller misalignments play a factor in the sudden increase in the bearing operating temperature. When a roller is caught misaligned in a fully loaded railcar scenario, the pivoting motion of the roller in the cage is limited, which increases the friction between the bearing internal components, leading to an abrupt rise in the bearing operating temperature. Once the rollers re-align and start rotating normally, the bearing operating temperature starts to slowly settle down to its normal steady state operating condition. Since the FEM cannot capture the roller misalignment behavior, the transient FEM temperatures follow normal heating trends based on the heat generation within the bearing. The aforementioned explanation is supported by the laboratory acquired transient temperature trends exhibited by the bearing in Case 7 through Case 10. In each of those four cases, the bearing operating temperature experiences abrupt

heating caused by roller misalignment but eventually settles down and reaches a steady state value that is within 4°C (7°F) or less of the FEM simulation results.

Note that roller misalignment in healthy (defect-free) bearings is usually caused by the viscous grease used to lubricate the railroad bearings. The grease is more viscous at lower temperatures and therefore it induces more frictional heating as the rollers are trying to push their way through it. However, as roller misalignment occurs, the generated frictional heating also affects the grease by lowering its viscosity and making it more liquid-like. Once this happens, the rollers tend to re-align and the thinner grease circulates easier around the rollers providing a cooling effect. The combination of the rollers re-aligning and the grease becoming less viscous is responsible for the bearing operating temperature settling down and reaching a steady state condition.

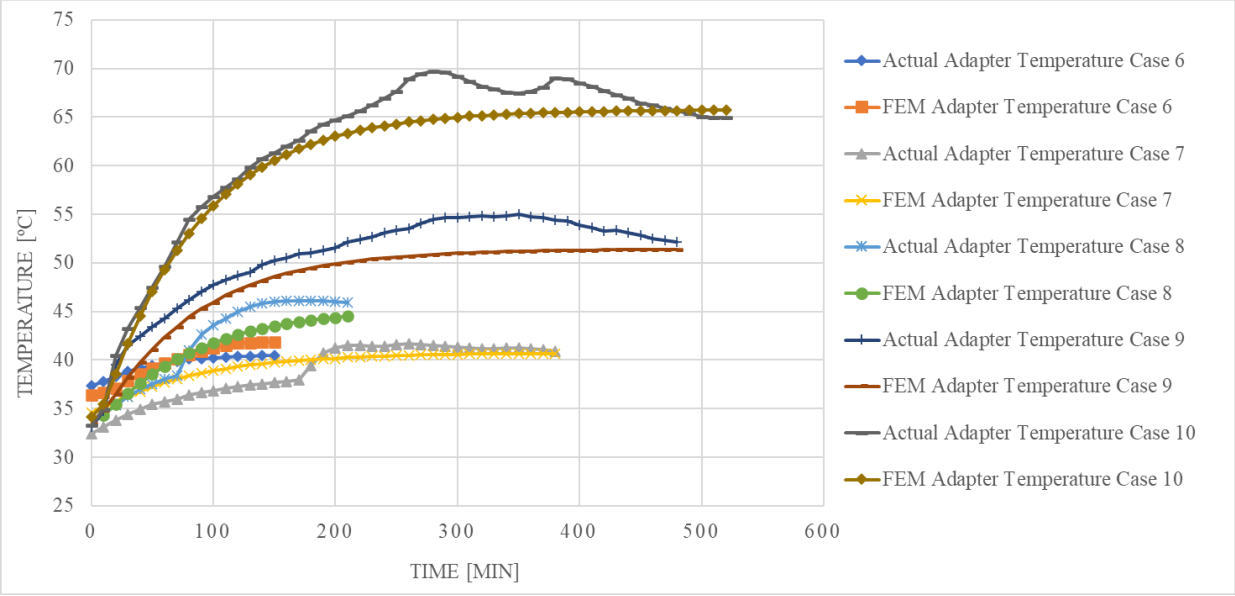

Figure 31: Adapter Operating Temperature Master Plot at Fully Loaded Railcar Scenario

Figure 31 presents the adapter temperatures for all five cases run under the fully loaded (100% load) railcar condition. As expected, the adapter followed the same trend as the bearing

since it receives the heat generated by the bearing. The laboratory acquired adapter temperatures for all five cases studied exhibited similar profiles to the corresponding bearing operating temperatures but to a lesser degree of variation. In fact, the experimentally obtained steady state adapter temperatures for all five cases explored were within less than 2°C (~4°F) from the FEM simulation results. Detailed comparisons including percent error calculations are provided in the Appendix.

In general, it can be observed that the developed FEM was accurate and reliable in estimating both the transient behavior and the steady state adapter temperature to within 10% error even with the abnormal heating patterns of the bearing. The model is much more accurate when the bearing exhibits normal heat generation trends.

5.2 Validation of Lumped Capacitance Assumption

The assumption of treating the bearing adapter as a lumped capacitance body was proven theorically and analytically in Chapter III. However, now that a robust, experimetally validated FEM has been developed, it can be used to assess and verify the lumped capacitance assumption made regarding the bearing adapter. For that purpose, two cases were selected to observe the maximum temperature difference within the adapter. The two selected cases were Case 1 which generated the least amount of heating and Case 10 which resulted in the higest operating temperatures. In Case 1, the test bearing speed was increased from 40 to 56 km/h while operating at an empty railcar load (17% load), whereas, in Case 10, the test bearing speed was increased from 40 to 137 km/h while operating under a fully loaded railcar (100% load).

As depicted in Figure 32 and Figure 33, the maximum temperature difference within the adapter for Case 1 and Case 10 is 1ºC (2ºF) and 3°C (5°F), respectively. These results confirm the analysis presented in Chapter III and demonstrate that the railroad bearing adapter can be

treated as a lumped capacitance body for the purposes of transient thermal and proved two things, namely: the accuracy of the proposed FEM, and the assumption of treating the bearing adapter as a lumped capacitance body for the purposes of transient thermal analyses.

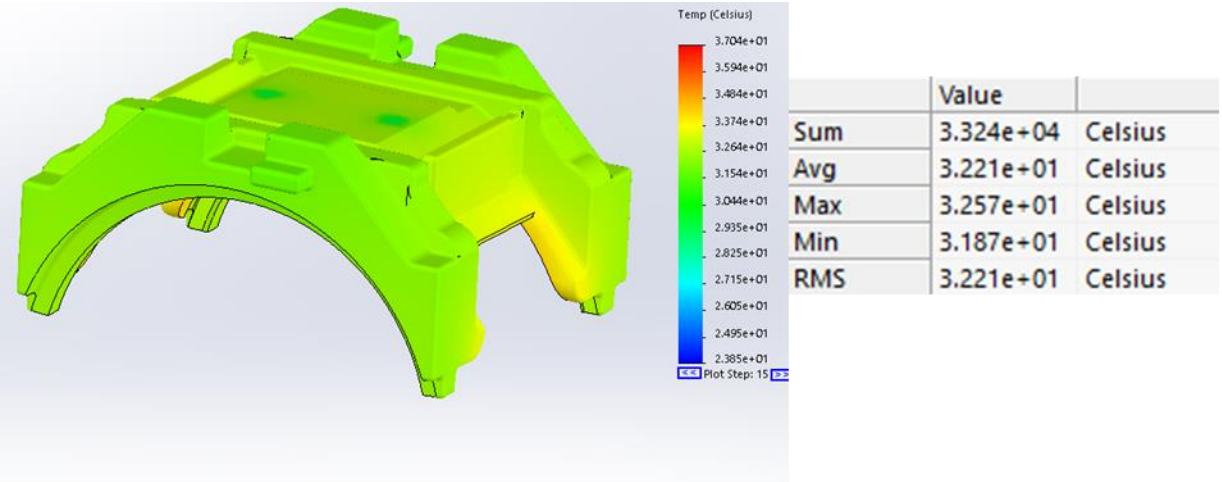

	Value	
Sum	3.324e+04	Celsius
Avg	3.221e+01	Celsius
Max	3.257e+01	Celsius
Min	3.187e+01	Celsius
RMS	3.221e+01	Celsius

Figure 32: Adapter Thermal Distribution (Best Case Scenario)

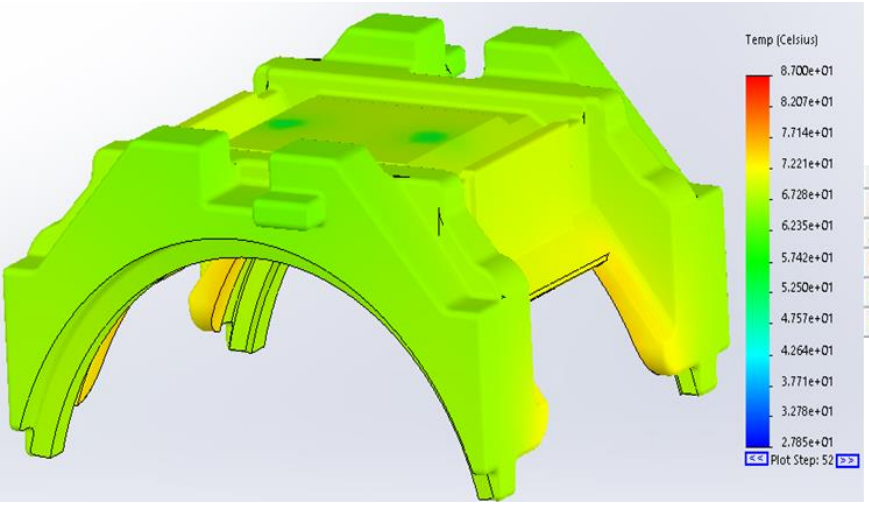

	Value	
Sum	6.791e+04	Celsius
Avg	6.580e+01	Celsius
Max	6.716e+01	Celsius
Min	6.443e+01	Celsius
RMS	6.581e+01	Celsius

Figure 33: Adapter Thermal Distribution (Worst Case Scenario)

5.3 Bearing and Adapter Time Constants

The last remaining question to be addressed by this study involves the thermal lag between the bearing and the adapter, which is a very crucial piece of information for developers of onboard temperature sensors. When designing sensors to monitor the conditions of wheels and bearings, some of the questions that are asked include: where should the sensor be mounted? What is the correlation between the bearing operating temperature and the adapter temperature? And how quickly does the adapter react to changes in the bearing temperature? The data presented in this section aims to answer that last question.

To do so, the time constants derived from each of the ten case scenarios investigated in this study were calculated for both the bearing and the adapter operating temperatures acquired experimentally and through the FEM simulations. Table 6 and Table 7 provide the time constant information for the bearing and the adapter, respectively, for the two loading conditions of an empty railcar (17% load) and a fully loaded railcar (100%).

Table 6: Bearing Time Constants

Bearing								
Empty Railcar (17% load)								
Speed Transitions [km/h]	T_i [°C]	T_f [°C]	T_τ [°C]	τ_{act} [min]	T_i [°C]	T_f [°C]	T_τ [°C]	τ_{FEM} [min]
40 - 56	32.7	34.8	34.0	52.6	34.0	35.5	34.9	47.5
40 - 72	32.0	38.2	36.0	65.9	33.8	37.7	36.3	61.4
40 - 89	32.8	43.2	39.4	104.6	32.9	41.9	38.6	70.7
40 - 106	35.7	62.0	52.4	79.7	34.4	60.7	51.0	68.5
40 - 137	33.0	73.6	58.7	140.7	35.5	67.8	55.9	69.8
Average				**88.7**				**63.6**
Fully Loaded Railcar (100% load)								
Speed Transitions [km/h]	T_i [°C]	T_f [°C]	T_τ [°C]	τ_{act} [min]	T_i [°C]	T_f [°C]	T_τ [°C]	τ_{FEM} [min]
40 - 56	44.0	49.0	47.2	41.7	40.2	47.5	44.8	63.5
40 - 72	37.3	50.9	45.9	171.7	40.6	48.4	45.5	69.5
40 - 89	36.4	58.0	50.0	84.3	39.1	53.7	48.3	62.4
40 - 106	38.2	66.3	56.0	65.4	39.0	62.6	53.9	72.6
40 - 137	38.1	83.0	66.5	71.1	39.7	82.2	66.6	76.2
Average				**86.8**				**68.8**

Table 7: Adapter Time Constants

Adapter								
Empty Railcar (17% load)								
Speed Transitions [km/h]	T_i [°C]	T_f [°C]	T_τ [°C]	τ_{act} [min]	T_i [°C]	T_f [°C]	T_τ [°C]	τ_{FEM} [min]
40 - 56	29.8	31.0	30.6	56.3	31.5	32.6	32.2	67.5
40 - 72	29.2	33.6	31.9	71.0	31.4	34.2	33.2	75.9
40 - 89	29.6	37.4	34.5	108.1	30.7	37.9	35.3	83.0
40 - 106	30.8	50.6	43.3	108.3	31.8	52.0	44.6	82.9
40 - 137	29.6	56.9	46.9	139.9	32.7	57.5	48.4	83.5
Average				**96.7**				**78.6**
Fully Loaded Railcar (100% load)								
Speed Transitions [km/h]	T_i [°C]	T_f [°C]	T_τ [°C]	τ_{act} [min]	T_i [°C]	T_f [°C]	T_τ [°C]	τ_{FEM} [min]
40 - 56	37.4	40.5	39.4	47.7	36.4	41.8	39.8	62.3
40 - 72	32.5	40.9	37.8	160.5	34.6	40.7	38.5	85.0
40 - 89	33.7	45.9	41.4	82.6	33.5	44.5	40.4	74.8
40 - 106	33.2	52.2	45.2	68.9	33.5	51.4	44.8	84.0
40 - 137	33.3	65.0	53.3	75.0	34.1	65.7	54.1	87.0
Average				**86.9**				**78.6**

In Table 6 and Table 7, T_i is the initial temperature, T_f is the final steady state temperature, T_τ is the time constant corresponding temperature, τ_{act} is the time constant derived from the laboratory data, and τ_{FEM} is the time constant obtained from the FEM simulation results. Note that the time constant corresponding temperature was calculated by finding the temperature value equivalent to 63.2% of the total transient temperature step change, as shown by Equation (9),

$$T_\tau = T_i + 0.632 \times (T_f - T_i) \tag{9}$$

then, to find the actual (τ_{act}) and simulated (τ_{FEM}) time constants, the calculated temperature was matched to the corresponding time the bearing or adapter needed to reach that temperature

Since the test bearing exhibited some abnormal behavior caused by random roller misalignments when the speed was suddenly increased from a low speed of 40 km/h to higher operating speeds, it was decided to calculate the average time constant for all five cases explored under an empty railcar load and those carried out under a full railcar load, as listed in Table 6 and Table 7. Ideally, the time constant will increase proportionally to the jump in operating speed, which is the case for the FEM simulations which do not account for the abnormal bearing operation. Nevertheless, the average time constant values seem to follow a very logical trend.

Examining Table 6, the actual bearing time constant at an empty railcar condition (17% load) had an average of 88.7 minutes for all five cases studied. In contrast, the FEM time constant had an average of 63.6 minutes, which is explained by the fact that the FEM cannot predict the abnormal bearing behavior because only an average motor power can be input into the model. Looking at the fully loaded railcar condition (100% load), the bearing time constant had an average of 86.8 minutes, whereas the FEM time constant average was 68.8 minutes for all five cases examined.

Table 7 introduces the adapter time constants for each speed variation and loading scenario for both laboratory testing and FEM. For the empty railcar scenario (17% load), the average time constant was 96.7 minutes, while the average FEM time constant was found to be 78.6 minutes. When the load was increased to the full railcar scenario (100% load), the average time constant for the laboratory data was 86.9 minutes, while the average FEM time constant was 78.6 minutes.

The thermal lag was calculated by subtracting the bearing time constant from the adapter time constant for both loading scenarios. For the empty railcar scenario (17% load), the average experimental time lag was found to be 8 minutes. Meaning, if there is a sudden increase in the bearing operating temperature, the adapter will sense that change in less than 10 minutes. On the other hand, the average FEM thermal lag had a value of 15 minutes. Note that the FEM is a static model and assumes a uniform heat generation within the bearing given the limitations on how the actual motor power can be input into the model. In reality, the bearing may experience abnormal heat generation patterns based on random roller misalignments that can occur if triggered by either the viscous grease or the presence of a defect on any of the bearing raceways. Now, looking at the experimental results for the fully loaded railcar scenario (100% load), it appears like the adapter will instantly sense changes in the bearing operating temperature. This is not surprising given that, at full load, the adapter is firmly pressed against the bearing cup surface, and since the adapter acts like a lumped capacitance body (as proven in this thesis), any heat transfer from the bearing will be immediately detected by the adapter. Again, as expected, the FEM average thermal lag for the fully loaded railcar scenario was more conservative (~ 10 minutes) given that the model predicts normal bearing behavior.

Regardless of the small discrepancies between the actual and model thermal lag values, the information present here is valuable since it provides the rail industry with realistic estimates of the thermal behavior of the adapter in response to sudden changes in the heat generation within the railroad bearing. More importantly, this data is based on operating conditions the bearings and adapters will experience in rail service.

CHAPTER VI

CONCLUSION

Railroad bearings may be removed from service for several reasons including faulty equipment triggering a wayside detection system, or as part of a wheel-axle replacement due to a wheel defect. Existing wayside condition monitoring systems are reactive in nature, in that they normally detect defective bearings that are operating above predetermined thresholds. This process leaves room for error given that non-verified bearings can fail without any detectable signs, causing them to be overlooked. Hot-Box Detectors (HBDs) solely rely on temperature measurements and are not effective at identifying defective bearings during early stages of deterioration since the operating temperature of these bearings is usually comparable to that of defect-free (healthy) bearings. These shortcomings have prompted the slow shift to onboard sensor technology. Therefore, the University Transportation Center for Railway Safety (UTCRS) developed a wireless onboard condition monitoring sensor module which actively monitors the temperature and vibration levels of a bearing from its affixed position on the corresponding bearing adapter. However, this introduces a thermal lag between the bearing cup (outer ring) and bearing adapter that has not been previously researched.

A transient heat transfer analysis was performed to obtain the thermal distribution between the bearing cup (outer ring) and the adapter to prove if the bearing adapter can be treated as a lumped capacitance body. This was proven with a Biot number of 0.019, which

satisfies the criteria for Bi < 0.1. It is crucial to treat the adapter as a lumped capacitance body for the wireless onboard monitoring systems because it allows them to be placed anywhere the adapter geometry permits. This will help predict the bearing operating temperature at any loading and speed variation.

This finding was validated through heat transfer analytical calculations, experimental testing and an experimentally validated transient finite element model (FEM). The devised model helped to better understand the heat distribution among the bearing components at any instance in time and proved the lumped capacitance assumption. The FEM was tested with four commonly used rail track speeds and one extreme outlying speed to check the reliability of the model at different speed and loading conditions. The proposed FEM in this thesis utilizes the average input motor power from experimental data, resulting in a higher degree of fidelity, and predicts the transient and steady-state temperatures for the bearing and the adapter.

The thermal contact resistance between the bearing adapter and the polymer pad had a value of 0.02 $m^{2} \cdot K \cdot W^{-1}$ when applying empty railcar conditions (17% load) and was experimentally validated through five speed variations. The heat transfer calculations were validated by the FEM that provided the heat distribution between the front and back face of the adapter, exhibiting a temperature difference less than 3°C (5°F) in Case 10, denoted as the worst-case scenario. However, this model included some limitations such as the absence of a transient input motor power. Having this feature would have allowed a greater degree of accuracy in the model, closer mimicking any abnormal bearing behavior present in the test railroad bearing.

Lastly, the time constants were calculated to obtain the thermal lag for the empty railcar (17% load) and the fully loaded railcar (100%). As found in this study, the time lag between the bearing and the adapter is less than 10 minutes when the railcar is empty (17% load) and less

than a minute when the railcar is fully loaded (100% load). The heat is transferred almost instantaneously on a fully loaded railcar scenario (100% load) because the adapter is firmly pressed against the bearing cup surface, as opposed to the unloaded railcar scenario (17% load). The finding in this thesis can be used as the foundation for future work in providing realistic estimates for the operating temperatures of the bearing and the adapter that compensate for the associated thermal lag.

REFERENCES

[1] J. Steets, B.J. Chan, C. Sandu, "Multibody Dynamics Approach to the Modeling of Friction Wedge Elements for Freight Train Suspensions. I: Theory." Journal of Transportation Engineering, August 2010

[2] C. Tarawneh, L. Sotelo, A. Villarreal, N. de los Santos, R. Lechtenberg, R. Jones," Temperature Profiles of Railroad Tapered Bearings with Defective Inner and Outer Rings." Proceedings of the 2016 Joint Rail Conference, April 12-15, 2016, Columbia, SC, USA

[3] Voestalpine, "Phoenix MB Intelligent Rolling Stock Monitoring, Hot Box and Hot Wheel Detection with Multi Beam Technology", Voestalpine Signaling, Germany, 2014

[4] H. Barren, "Wayside Detection – Component Interactions and Composite Rules.", Rail Transportation Division Fall Conference (RTDF), Forth Worth, TX, 2009

[5] C. Tarawneh, J. Montalvo, B. Wilson, "Defect Detection in Freight Railcar Tapered-Roller Bearings Using Vibration Techniques." Rail. Eng. Science 29, pp. 42-58, 2021

[6] T. Sultana and L. Stabler, "Condition-Based Maintenance with Detectors," in IHHA, Perth, Australia, 2015

[7] S. Karunakaran and T. W. Snyder, "Bearing Temperature Performance in Freight Cars,": Proceedings Bearing Research Symposium, sponsored by the AAR Research Program in conjunction with the ASME RTD Fall Conference, Chicago, IL, September 11-12, 2007

[8] C. Tarawneh, J. Aranda, V. Hernandez, S. Crown, J. Montalvo, "An Investigation into Wayside Hot-Box Detector Efficacy and Optimization," International Journal of Rail Transportation, 2020

[9] H. Wang, T.F. Conry, C. Cusano, "Effects of Cone/Axle Rubbing Due to Roller Bearing Seizure on the Thermomechanical Behavior of a Railroad Axle," Journal of Tribology, Vol. 118, pp. 311-319, 1996

[10] C. M. Tarawneh, B. M. Wilson, K. D. Cole, and M. Reed, "A Metallurgical and Experimental Investigation into Sources of Warm Bearing Trending," Proceedings of the 2008 IEEE/ASME Join Rail Conference, Wilmington, DE, April 22-23, 2008

[11] C. M. Tarawneh, K. D. Cole, B. M. Wilson, and F. Alnaimat, “Experiments and Models for the Response of Railroad Tapered Roller Bearings,” International J. Heat Mass Transfer, 51, pp. 5794-5803, 2008

[12] C. Tarawneh, A. Fuentes, J. Kypuros, L. A. Navarro, A. G. Vaipan, “Thermal Modeling of a Railroad Tapered-Roller Bearing Using Finite Element Analysis,” Journal of Thermal Science and Engineering Applications, Volume 4, September 2012

[13] B. Wilson, A. Martin, “Bearing Condition Monitoring Using Wireless Technology to Reduce the Risk of Bearing Failure,” Proceedings of the ASME 2012 Rail Transportation Division Fall Technical Conference, Oct 16-17, 2012, Omaha, Nebraska, USA

[14] A. Zagouris, “Implementation of Wireless Temperature Sensors for Continuous Monitoring of Railroad Bearings,” Master’s Thesis, Department of Mechanical Engineering, The University of Texas Pan-American, May 2012.

[15] Incorpera, F.P, et al., “Fundamentals of Heat and Mass Transfer,” 6 ed2007, Hoboken, NJ: John Wiley & Sons, Inc.

[16] O. Rodriguez, “The Effect of Heat Generation in the Railroad Bearing Thermoplastic Elastomer Suspension Element on the Thermal Behavior of Railroad Bearing Assembly”, Master’s Thesis, Department of Mechanical Engineering, The University of Texas Rio Grande Valley, May 2018

APPENDIX

APPENDIX

Table 8: Case 1 Average Motor Power Calculations

40 km/h (25 mph)				
Motor Power [W]	Power per Bearing [W]	Power per Roller [W]	Roller Area [m^2]	Heat Flux per Roller [$W \cdot m^{-2}$]
699.10	174.78	3.80	3.36×10^{-3}	1130.36

56 km/h (35 mph)				
Motor Power [W]	Power per Bearing [W]	Power per Roller [W]	Roller Area [m^2]	Heat Flux per Roller [$W \cdot m^{-2}$]
825.60	206.40	4.49	3.36×10^{-3}	1334.89

Table 9: Case 1 Bearing Temperature Profile

Case 1			
Bearing Operating Temperature			
R''_{tc} = 0.0055 [$m^2 \cdot K \cdot W^{-1}$]			
Actual [ºC]	FEM Simulation [ºC]	Time [min]	Percent Error [%]
32.73	34.01	0	3.91
32.92	34.30	10	4.18
33.23	34.50	20	3.85
33.47	34.67	30	3.57
33.71	34.81	40	3.25
33.95	34.93	50	2.90
34.13	35.04	60	2.65
34.28	35.13	70	2.48
34.40	35.21	80	2.35
34.51	35.29	90	2.25
34.61	35.35	100	2.12
34.64	35.38	110	2.14
34.69	35.40	120	2.07

34.70	35.45	130	2.17
34.72	35.50	140	2.25
34.75	35.53	150	2.25

Table 10: Case 1 Adapter Temperature Profile

Case 1			
Adapter Operating Temperature			
R''_{tc} = 0.02 [$m^2 \cdot K \cdot W^{-1}$]			
Actual [ºC]	FEM Simulation [ºC]	Time [min]	Percent Error [%]
29.78	31.52	0	5.84
29.78	31.59	10	5.57
30.02	31.70	20	5.60
30.17	31.82	30	5.48
30.31	31.94	40	5.38
30.48	32.04	50	5.13
30.67	32.14	60	4.78
30.77	32.22	70	4.70
30.84	32.30	80	4.72
30.98	32.36	90	4.47
30.97	32.42	100	4.69
30.98	32.44	110	4.71
30.98	32.47	120	4.79
30.99	32.52	130	4.94
31.00	32.56	140	5.03
31.02	32.59	150	5.06

Table 11: Case 2 Average Motor Power Calculations

40 km/h (25 mph)				
Motor Power [W]	Power per Bearing [W]	Power per Roller [W]	Roller Area [m^2]	Heat Flux per Roller [$W \cdot m^{-2}$]
685.10	171.28	3.72	3.36×10^{-3}	1107.72

72 km/h (45 mph)				
Motor Power [W]	Power per Bearing [W]	Power per Roller [W]	Roller Area [m^2]	Heat Flux per Roller [$W \cdot m^{-2}$]
982.70	245.68	5.34	3.36×10^{-3}	1588.90

Table 12: Case 2 Bearing Temperature Profile

Case 2			
Bearing Operating Temperature			
$R_{tc}^{"}$ = 0.0055 [$m^2 \cdot K \cdot W^{-1}$]			
Actual [ºC]	FEM Simulation [ºC]	Time [min]	Percent Error [%]
32.01	33.81	0	5.61
32.59	34.53	10	5.94
33.34	35.02	20	5.06
34.05	35.41	30	4.00
34.65	35.74	40	3.13
35.24	36.03	50	2.25
35.73	36.27	60	1.53
36.19	36.49	70	0.83
36.57	36.68	80	0.31
36.95	36.85	90	0.25
37.26	37.00	100	0.70
37.51	37.13	110	1.01
37.71	37.25	120	1.23
37.87	37.35	130	1.39
37.97	37.44	140	1.41
38.08	37.51	150	1.48
38.16	37.59	160	1.49
38.21	37.65	170	1.48
38.24	37.70	180	1.42

Table 13: Case 2 Adapter Temperature Profile

Case 2			
Adapter Operating Temperature			
R''_{tc} = 0.02 [$m^2 \cdot K \cdot W^{-1}$]			
Actual [ºC]	FEM Simulation [ºC]	Time [min]	Percent Error [%]
29.15	31.37	0	7.62
29.42	31.57	10	7.30
29.87	31.85	20	6.63
30.33	32.15	30	6.00
30.74	32.43	40	5.48
31.16	32.68	50	4.86
31.54	32.90	60	4.31
31.89	33.10	70	3.79
32.16	33.27	80	3.46
32.42	33.42	90	3.09
32.71	33.56	100	2.61
32.88	33.68	110	2.44
33.02	33.78	120	2.30
33.19	33.87	130	2.06
33.31	33.96	140	1.95
33.47	34.03	150	1.67
33.53	34.09	160	1.66
33.58	34.15	170	1.70
33.57	34.20	180	1.88

Table 14: Case 3 Average Motor Power Calculations

40 km/h (25 mph)				
Motor Power [W]	Power per Bearing [W]	Power per Roller [W]	Roller Area [m^2]	Heat Flux per Roller [$W \cdot m^{-2}$]
620.80	155.20	3.37	3.36×10^{-3}	1003.76

89 km/h (55 mph)				
Motor Power [W]	Power per Bearing [W]	Power per Roller [W]	Roller Area [m^2]	Heat Flux per Roller [$W \cdot m^{-2}$]
1114.20	278.55	6.06	3.36×10^{-3}	1801.52

Table 15: Case 3 Bearing Temperature Profile

Case 3			
Bearing Operating Temperature			
R''_{tc} = 0.0055 [$m^2 \cdot K \cdot W^{-1}$]			
Actual [ºC]	FEM Simulation [ºC]	Time [min]	Percent Error [%]
32.76	32.87	0	0.36
33.77	34.41	10	1.89
34.73	35.45	20	2.06
35.58	36.27	30	1.95
36.33	36.97	40	1.76
36.96	37.58	50	1.67
37.54	38.11	60	1.50
38.05	38.57	70	1.36
38.50	38.98	80	1.24
38.90	39.34	90	1.15
39.22	39.66	100	1.13
39.52	39.94	110	1.05
39.80	40.19	120	0.97
39.95	40.40	130	1.13
40.23	40.59	140	0.90
40.39	40.76	150	0.91
40.51	40.91	160	0.97
40.66	41.04	170	0.94
40.81	41.15	180	0.84
40.95	41.25	190	0.74
41.07	41.34	200	0.66
41.27	41.42	210	0.37
41.45	41.49	220	0.08
41.55	41.55	230	0.00
41.63	41.61	240	0.06
41.81	41.65	250	0.39
42.02	41.69	260	0.78
42.19	41.73	270	1.09
42.29	41.76	280	1.25
42.37	41.79	290	1.39
42.44	41.81	300	1.49
42.67	41.83	310	1.95
42.88	41.85	320	2.40
43.00	41.87	330	2.62

43.08	41.88	340	2.77
43.11	41.90	350	2.81
43.14	41.91	360	2.85
43.20	41.92	370	2.97

Table 16: Case 3 Adapter Temperature Profile

Case 3			
Adapter Operating Temperature			
R''_{tc} = 0.02 [$m^2 \cdot K \cdot W^{-1}$]			
Actual [ºC]	FEM Simulation [ºC]	Time [min]	Percent Error [%]
29.62	30.66	0	3.51
30.23	31.31	10	3.56
30.91	32.02	20	3.60
31.56	32.71	30	3.65
32.17	33.34	40	3.65
32.63	33.89	50	3.86
33.04	34.39	60	4.08
33.41	34.82	70	4.23
33.75	35.20	80	4.30
34.04	35.53	90	4.38
34.33	35.83	100	4.37
34.54	36.09	110	4.50
34.76	36.32	120	4.48
34.91	36.52	130	4.60
35.04	36.69	140	4.70
35.20	36.85	150	4.70
35.28	36.98	160	4.81
35.50	37.10	170	4.50
35.59	37.21	180	4.56
35.75	37.30	190	4.33
35.80	37.38	200	4.40
35.94	37.45	210	4.21
36.17	37.52	220	3.72
36.15	37.57	230	3.93
36.25	37.62	240	3.77
36.46	37.67	250	3.33
36.65	37.70	260	2.85

36.79	37.74	270	2.58
36.85	37.77	280	2.51
36.90	37.79	290	2.40
36.94	37.82	300	2.38
37.02	37.84	310	2.21
37.08	37.85	320	2.09
37.15	37.87	330	1.94
37.22	37.88	340	1.78
37.23	37.89	350	1.78
37.25	37.90	360	1.75
37.36	37.91	370	1.47

Table 17: Case 4 Average Motor Power Calculations

40 km/h (25 mph)				
Motor Power [W]	Power per Bearing [W]	Power per Roller [W]	Roller Area [m^2]	Heat Flux per Roller [$W \cdot m^{-2}$]
727.40	181.85	3.95	3.36×10^{-3}	1176.12

106 km/h (66 mph)				
Motor Power [W]	Power per Bearing [W]	Power per Roller [W]	Roller Area [m^2]	Heat Flux per Roller [$W \cdot m^{-2}$]
2432.50	608.13	13.22	3.36×10^{-3}	3933.05

Table 18: Case 4 Bearing Temperature Profile

Case 4			
Bearing Operating Temperature			
$R_{tc}^{"}$ = 0.0055 [$m^2 \cdot K \cdot W^{-1}$]			
Actual [ºC]	FEM Simulation [ºC]	Time [min]	Percent Error [%]
35.70	34.42	0	3.57
41.73	39.02	10	6.48
45.16	42.11	20	6.76
47.00	44.52	30	5.28
47.79	46.55	40	2.59
49.17	48.31	50	1.74
50.56	49.85	60	1.41

51.49	51.20	70	0.57
52.43	52.38	80	0.10
52.87	53.42	90	1.04
54.17	54.34	100	0.31
54.77	55.15	110	0.70
55.78	55.86	120	0.14
56.35	56.45	130	0.17
57.00	57.03	140	0.06
57.53	57.52	150	0.02
59.06	57.94	160	1.90
60.05	58.32	170	2.89
60.65	58.65	180	3.30
61.52	58.94	190	4.19
62.01	59.20	200	4.54
62.16	59.42	210	4.41
62.17	59.62	220	4.10
61.73	59.79	230	3.13
61.92	59.94	240	3.19
61.94	60.08	250	2.99
62.07	60.20	260	3.01
62.57	60.31	270	3.62
62.33	60.40	280	3.09
62.14	60.48	290	2.67
62.38	60.55	300	2.93
62.39	60.61	310	2.85
62.19	60.67	320	2.44
62.04	60.72	330	2.13

Table 19: Case 4 Adapter Temperature Profile

Case 4			
Adapter Operating Temperature			
R''_{tc} = 0.02 [$m^2 \cdot K \cdot W^{-1}$]			
Actual [ºC]	FEM Simulation [ºC]	Time [min]	Percent Error [%]
30.80	31.83	0	3.34
33.90	33.38	10	1.53
36.30	35.32	20	2.71
37.31	37.25	30	0.17

38.41	39.02	40	1.59
39.03	40.61	50	4.06
39.78	42.00	60	5.58
40.71	43.24	70	6.21
41.39	44.32	80	7.07
42.10	45.28	90	7.55
42.76	46.12	100	7.85
43.41	46.86	110	7.95
43.98	47.51	120	8.02
44.67	48.08	130	7.63
45.31	48.59	140	7.24
45.80	49.03	150	7.05
47.09	49.42	160	4.94
48.23	49.76	170	3.17
49.17	50.07	180	1.83
49.99	50.33	190	0.68
50.23	50.57	200	0.67
50.54	50.77	210	0.45
50.53	50.96	220	0.85
50.46	51.12	230	1.31
50.56	51.26	240	1.39
50.69	51.38	250	1.37
50.88	51.49	260	1.20
51.02	51.59	270	1.12
51.11	51.67	280	1.10
50.90	51.74	290	1.65
51.13	51.81	300	1.32
50.97	51.87	310	1.76
50.76	51.92	320	2.28
50.63	51.96	330	2.62

Table 20: Case 5 Average Motor Power Calculations

40 km/h (25 mph)				
Motor Power [W]	Power per Bearing [W]	Power per Roller [W]	Roller Area [m^2]	Heat Flux per Roller [$W \cdot m^{-2}$]
802.40	200.60	4.36	3.36×10^{-3}	1297.38

137 km/h (85 mph)				
Motor Power [W]	Power per Bearing [W]	Power per Roller [W]	Roller Area [m^2]	Heat Flux per Roller [$W \cdot m^{-2}$]
2840.70	710.18	15.44	3.36×10^{-3}	4593.06

Table 21: Case 5 Bearing Temperature Profile

Case 5			
Bearing Operating Temperature			
$R_{tc}^{"}$ = 0.0055 [$m^2 \cdot K \cdot W^{-1}$]			
Actual [ºC]	FEM Simulation [ºC]	Time [min]	Percent Error [%]
32.98	35.51	0	7.68
40.14	41.12	10	2.43
41.85	44.86	20	7.18
43.83	47.80	30	9.05
45.59	50.28	40	10.29
47.09	52.42	50	11.31
48.64	54.30	60	11.64
50.02	55.94	70	11.84
51.27	57.38	80	11.92
52.50	58.65	90	11.72
53.76	59.77	100	11.17
54.96	60.61	110	10.28
56.19	61.62	120	9.66
57.44	62.38	130	8.61
58.55	63.05	140	7.69
60.74	63.64	150	4.77
63.70	64.16	160	0.72
65.36	64.62	170	1.13
66.75	65.02	180	2.58
68.27	65.38	190	4.24

69.95	65.69	200	6.09
71.14	65.96	210	7.28
72.13	66.20	220	8.22
73.06	66.41	230	9.10
74.16	66.60	240	10.19
74.50	66.76	250	10.39
74.81	66.91	260	10.55
75.10	67.04	270	10.74
75.42	67.15	280	10.96
75.29	67.25	290	10.68
75.22	67.34	300	10.48
74.95	67.41	310	10.06
74.97	67.48	320	9.99
74.90	67.54	330	9.82
74.66	67.59	340	9.46
74.25	67.64	350	8.91
73.94	67.68	360	8.47
74.00	67.72	370	8.49
73.75	67.75	380	8.14
73.64	67.78	390	7.97

Table 22: Case 5 Adapter Temperature Profile

Case 5			
Adapter Operating Temperature			
R''_{tc} = 0.02 [$m^2 \cdot K \cdot W^{-1}$]			
Actual [ºC]	FEM Simulation [ºC]	Time [min]	Percent Error [%]
29.6	32.66	0	10.34
34.07	34.60	10	1.56
35.42	36.99	20	4.44
36.89	39.35	30	6.67
38.15	41.52	40	8.82
39.09	43.45	50	11.15
40.46	45.16	60	11.61
41.51	46.67	70	12.43
42.22	47.99	80	13.68
42.97	49.16	90	14.41
43.70	50.18	100	14.83

44.50	51.09	110	14.82
45.26	51.88	120	14.63
46.11	52.58	130	14.03
46.91	53.19	140	13.38
47.58	53.73	150	12.93
48.52	54.21	160	11.72
49.69	54.63	170	9.94
50.69	55.00	180	8.50
51.80	55.32	190	6.80
52.95	55.61	200	5.02
53.63	55.89	210	4.21
54.61	56.08	220	2.69
55.74	56.27	230	0.95
56.60	56.45	240	0.27
57.07	56.60	250	0.83
57.35	56.73	260	1.08
57.35	56.85	270	0.88
57.30	56.95	280	0.61
57.35	57.04	290	0.55
57.38	57.12	300	0.45
57.38	57.19	310	0.33
57.46	57.25	320	0.37
57.68	57.31	330	0.65
57.55	57.35	340	0.34
57.49	57.40	350	0.15
57.16	57.43	360	0.46
57.04	57.47	370	0.75
56.93	57.49	380	0.98
56.92	57.52	390	1.05

Table 23: Case 6 Average Motor Power Calculations

40 km/h (25 mph)				
Motor Power [W]	Power per Bearing [W]	Power per Roller [W]	Roller Area [m^2]	Heat Flux per Roller [$W \cdot m^{-2}$]
1056.00	264.00	5.74	3.36×10^{-3}	1707.42

56 km/h (35 mph)				
Motor Power [W]	Power per Bearing [W]	Power per Roller [W]	Roller Area [m^2]	Heat Flux per Roller [$W \cdot m^{-2}$]
1443.86	360.97	7.85	3.36×10^{-3}	2334.54

Table 24: Case 6 Bearing Temperature Profile

Case 6			
Bearing Operating Temperature			
$R_{tc}^{"}$ = 0.0055 [$m^2 \cdot K \cdot W^{-1}$]			
Actual [ºC]	FEM Simulation [ºC]	Time [min]	Percent Error [%]
41.97	40.18	0	4.27
43.15	40.93	10	5.14
44.04	41.82	20	5.02
44.67	42.68	30	4.46
45.13	43.42	40	3.78
45.54	44.07	50	3.24
45.86	44.63	60	2.68
46.08	45.12	70	2.09
46.30	45.56	80	1.60
46.48	45.94	90	1.17
46.61	46.28	100	0.70
46.70	46.58	110	0.26
46.88	46.84	120	0.08
46.94	47.07	130	0.29
46.95	47.27	140	0.68
46.98	47.45	150	1.00

Table 25: Case 6 Adapter Temperature Profile

Case 6			
Adapter Operating Temperature			
R''_{tc} = 0.01 [$m^2 \cdot K \cdot W^{-1}$]			
Actual [ºC]	FEM Simulation [ºC]	Time [min]	Percent Error [%]
37.39	36.40	0	2.65
37.79	36.71	10	2.86
38.35	37.10	20	3.26
38.86	37.86	30	2.58
39.19	38.55	40	1.65
39.46	39.16	50	0.75
39.71	39.69	60	0.06
39.85	40.16	70	0.77
40.10	40.57	80	1.16
40.12	40.94	90	2.03
40.22	41.25	100	2.56
40.29	41.53	110	3.08
40.36	41.78	120	3.52
40.41	41.80	130	3.44
40.46	41.82	140	3.36
40.50	41.83	150	3.28

Table 26: Case 7 Average Motor Power Calculations

40 km/h (25 mph)				
Motor Power [W]	Power per Bearing [W]	Power per Roller [W]	Roller Area [m^2]	Heat Flux per Roller [$W \cdot m^{-2}$]
1086.00	271.50	5.90	3.36×10^{-3}	1755.93

72 km/h (45 mph)				
Motor Power [W]	Power per Bearing [W]	Power per Roller [W]	Roller Area [m^2]	Heat Flux per Roller [$W \cdot m^{-2}$]
1560.45	390.11	8.48	3.36×10^{-3}	2523.06

Table 27: Case 7 Bearing Temperature Profile

Case 7			
Bearing Operating Temperature			
R''_{tc} = 0.0055 [$m^2 \cdot K \cdot W^{-1}$]			
Actual [ºC]	FEM Simulation [ºC]	Time [min]	Percent Error [%]
37.3	40.62	0	8.89
38.66	41.94	10	8.49
39.69	42.83	20	7.91
40.63	43.54	30	7.17
41.41	44.14	40	6.59
42.08	44.67	50	6.14
42.69	45.12	60	5.69
43.15	45.52	70	5.48
43.61	45.87	80	5.19
43.92	46.18	90	5.14
44.24	46.45	100	4.99
44.48	46.70	110	4.99
44.73	46.91	120	4.86
44.96	47.09	130	4.74
45.16	47.25	140	4.63
45.34	47.40	150	4.54
45.45	47.53	160	4.56
45.63	47.64	170	4.40
47.24	47.73	180	1.05
48.38	47.82	190	1.15
49.09	47.90	200	2.42
49.50	47.96	210	3.11
49.77	48.02	220	3.52
49.89	48.07	230	3.64
50.12	48.12	240	3.98
50.44	48.16	250	4.52
50.75	48.19	260	5.04
50.91	48.23	270	5.28
50.95	48.25	280	5.30
50.91	48.28	290	5.18
50.84	48.30	300	5.00
50.84	48.32	310	4.96
51.41	48.34	320	5.99
51.72	48.35	330	6.52
51.68	48.36	340	6.42

51.56	48.38	350	6.17
51.36	48.39	360	5.79
51.14	48.39	370	5.36
50.93	48.40	380	4.97

Table 28: Case 7 Adapter Temperature Profile

Case 7			
Adapter Operating Temperature			
$R_{tc}^{"}$ = 0.01 [$m^2 \cdot K \cdot W^{-1}$]			
Actual [ºC]	FEM Simulation [ºC]	Time [min]	Percent Error [%]
32.46	34.63	0	6.69
33.09	35.13	10	6.17
33.79	35.69	20	5.61
34.45	36.26	30	5.24
34.92	36.78	40	5.31
35.42	37.25	50	5.17
35.73	37.67	60	5.42
36.02	38.03	70	5.59
36.40	38.36	80	5.39
36.65	38.64	90	5.44
36.81	38.89	100	5.65
37.08	39.11	110	5.46
37.26	39.31	120	5.51
37.48	39.48	130	5.33
37.54	39.63	140	5.56
37.72	39.76	150	5.42
37.80	39.88	160	5.51
37.93	39.98	170	5.39
39.40	40.07	180	1.70
40.74	40.15	190	1.45
41.28	40.13	200	2.80
41.51	40.28	210	2.97
41.53	40.33	220	2.89
41.45	40.38	230	2.59
41.43	40.42	240	2.44
41.58	40.46	250	2.69
41.70	40.49	260	2.91

41.62	40.52	270	2.65
41.50	40.55	280	2.29
41.46	40.57	290	2.14
41.32	40.59	300	1.78
41.25	40.61	310	1.55
41.15	40.62	320	1.29
41.18	40.63	330	1.34
41.25	40.65	340	1.45
41.22	40.66	350	1.36
41.16	40.67	360	1.19
41.12	40.67	370	1.09
40.93	40.68	380	0.62

Table 29: Case 8 Average Motor Power Calculations

40 km/h (25 mph)				
Motor Power [W]	Power per Bearing [W]	Power per Roller [W]	Roller Area [m^2]	Heat Flux per Roller [$W \cdot m^{-2}$]
978.90	244.73	5.32	3.36×10^{-3}	1582.76

89 km/h (55 mph)				
Motor Power [W]	Power per Bearing [W]	Power per Roller [W]	Roller Area [m^2]	Heat Flux per Roller [$W \cdot m^{-2}$]
1992.16	498.04	10.83	3.36×10^{-3}	3221.08

Table 30: Case 8 Bearing Temperature Profile

Case 8			
Bearing Operating Temperature			
$R_{tc}^{"}$ = 0.0055 [$m^2 \cdot K \cdot W^{-1}$]			
Actual [ºC]	FEM Simulation [ºC]	Time [min]	Percent Error [%]
36.35	39.12	0	7.61
39.84	41.75	10	4.79
41.23	43.56	20	5.64
42.52	44.97	30	5.77
43.68	46.17	40	5.70

44.54	47.20	50	5.97
45.34	48.11	60	6.10
46.01	48.90	70	6.28
48.97	49.59	80	1.28
51.36	50.21	90	2.24
53.62	50.74	100	5.36
55.18	51.22	110	7.17
56.48	51.64	120	8.58
57.39	52.00	130	9.39
57.94	52.33	140	9.69
58.22	52.62	150	9.62
58.28	52.86	160	9.30
58.40	53.08	170	9.10
58.40	53.28	180	8.78
58.32	53.45	190	8.36
58.20	53.60	200	7.90
58.01	53.73	210	7.38

Table 31: Case 8 Adapter Temperature Profile

Case 8			
Adapter Operating Temperature			
R''_{tc} = 0.01 [$m^2 \cdot K \cdot W^{-1}$]			
Actual [ºC]	FEM Simulation [ºC]	Time [min]	Percent Error [%]
33.67	33.49	0	0.53
34.38	34.36	10	0.06
35.40	35.48	20	0.24
36.22	36.60	30	1.05
36.98	37.63	40	1.75
37.54	38.56	50	2.73
38.06	39.38	60	3.48
38.39	40.10	70	4.47
40.96	40.73	80	0.55
42.68	41.29	90	3.25
43.62	41.79	100	4.20
44.27	42.22	110	4.62
44.96	42.60	120	5.25
45.51	42.94	130	5.65

45.83	43.24	140	5.66
45.97	43.50	150	5.38
46.08	43.73	160	5.09
46.10	43.93	170	4.70
46.09	44.11	180	4.29
46.14	44.27	190	4.04
46.04	44.40	200	3.56
45.90	44.52	210	3.00

Table 32: Case 9 Average Motor Power Calculations

40 km/h (25 mph)				
Motor Power [W]	Power per Bearing [W]	Power per Roller [W]	Roller Area [m^2]	Heat Flux per Roller [$W \cdot m^{-2}$]
976.50	244.13	5.31	3.36×10^{-3}	1578.88

106 km/h (66 mph)				
Motor Power [W]	Power per Bearing [W]	Power per Roller [W]	Roller Area [m^2]	Heat Flux per Roller [$W \cdot m^{-2}$]
2444.64	611.16	13.29	3.36×10^{-3}	3952.68

Table 33: Case 9 Bearing Temperature Profile

Case 9			
Bearing Operating Temperature			
R''_{tc} = 0.0055 [$m^2 \cdot K \cdot W^{-1}$]			
Actual [ºC]	FEM Simulation [ºC]	Time [min]	Percent Error [%]
38.2	39.04	0	2.20
40.80	43.03	10	5.47
45.29	45.71	20	0.92
47.86	47.81	30	0.11
50.09	49.58	40	1.02
52.33	51.11	50	2.32
55.11	52.46	60	4.80
56.77	53.63	70	5.53
58.31	54.67	80	6.24

59.60	55.57	90	6.76
60.46	56.37	100	6.77
61.09	57.08	110	6.57
61.57	57.70	120	6.28
61.99	58.24	130	6.04
63.05	58.72	140	6.86
63.76	59.15	150	7.24
64.23	59.52	160	7.33
64.74	59.84	170	7.57
65.12	60.13	180	7.66
65.46	60.39	190	7.76
65.85	60.61	200	7.96
66.40	60.80	210	8.43
66.86	60.98	220	8.80
66.98	61.13	230	8.73
67.45	61.27	240	9.16
67.76	61.38	250	9.41
67.99	61.49	260	9.56
68.50	61.68	270	9.96
68.75	61.96	280	9.89
69.03	62.14	290	9.99
69.09	62.19	300	9.98
69.23	62.25	310	10.08
69.25	62.29	320	10.05
69.15	62.34	330	9.86
69.29	62.38	340	9.98
69.32	62.41	350	9.97
69.11	62.44	360	9.66
69.03	62.45	370	9.52
68.67	62.48	380	9.01
68.55	62.50	390	8.82
68.28	62.52	400	8.32
67.94	62.54	410	7.95
67.67	62.55	420	7.57
67.49	62.56	430	7.31
67.30	62.57	440	7.02
66.94	62.58	450	6.52
66.70	62.59	460	6.17
66.45	62.60	470	5.80

66.29	62.60	480	5.55

Table 34: Case 9 Adapter Temperature Profile

Case 9			
Adapter Operating Temperature			
R''_{tc} = 0.01 [$m^2 \cdot K \cdot W^{-1}$]			
Actual [ºC]	FEM Simulation [ºC]	Time [min]	Percent Error [%]
33.15	33.46	0	0.94
34.77	34.82	10	0.15
39.56	36.52	20	7.69
41.49	38.2	30	7.92
42.47	39.74	40	6.43
43.41	41.12	50	5.27
44.24	42.34	60	4.30
45.31	43.42	70	4.18
46.19	44.47	80	3.72
47.05	45.3	90	3.71
47.70	45.93	100	3.72
48.25	46.68	110	3.25
48.68	47.24	120	2.95
49.02	47.74	130	2.61
49.78	48.18	140	3.21
50.22	48.57	150	3.28
50.52	48.91	160	3.19
50.92	49.21	170	3.35
51.00	49.48	180	2.97
51.31	49.71	190	3.12
51.59	49.91	200	3.25
52.13	50.09	210	3.92
52.44	50.25	220	4.17
52.67	50.39	230	4.33
53.06	50.52	240	4.79
53.33	50.62	250	5.07
53.51	50.72	260	5.21
54.02	50.8	270	5.95
54.45	50.88	280	6.56
54.65	50.94	290	6.79

54.64	51	300	6.66
54.75	51.05	310	6.76
54.82	51.09	320	6.80
54.75	51.13	330	6.60
54.85	51.17	340	6.71
55.00	51.2	350	6.90
54.75	51.22	360	6.45
54.64	51.25	370	6.20
54.38	51.27	380	5.72
54.35	51.28	390	5.64
53.92	51.3	400	4.85
53.58	51.31	410	4.24
53.27	51.33	420	3.65
53.32	51.34	430	3.72
53.10	51.35	440	3.29
52.82	51.36	450	2.76
52.45	51.36	460	2.08
52.30	51.37	470	1.78
52.17	51.37	480	1.53

Table 35: Case 10 Average Motor Power Calculations

40 km/h (25 mph)				
Motor Power [W]	Power per Bearing [W]	Power per Roller [W]	Roller Area [m^2]	Heat Flux per Roller [$W \cdot m^{-2}$]
1014.00	253.50	5.51	3.36×10^{-3}	1639.51

137 km/h (85 mph)				
Motor Power [W]	Power per Bearing [W]	Power per Roller [W]	Roller Area [m^2]	Heat Flux per Roller [$W \cdot m^{-2}$]
3523.71	880.93	19.15	3.36×10^{-3}	5697.41

Table 36: Case 10 Bearing Temperature Profile

Case 10			
Bearing Operating Temperature			
$R_{tc}^{"}$ = 0.0055 [$m^2 \cdot K \cdot W^{-1}$]			
Actual [ºC]	FEM Simulation [ºC]	Time [min]	Percent Error [%]
38.09	39.69	0	4.19
40.99	42.95	10	4.78
46.40	47.87	20	3.16
51.00	51.73	30	1.44
54.97	54.99	40	0.03
58.49	57.81	50	1.17
62.53	62.27	60	0.43
66.22	65.43	70	1.19
68.90	67.32	80	2.29
70.53	69.99	90	0.76
71.97	71.46	100	0.70
73.27	72.75	110	0.71
74.78	73.89	120	1.20
76.34	74.89	130	1.90
77.51	75.77	140	2.25
78.58	76.54	150	2.60
79.55	77.22	160	2.92
80.69	77.83	170	3.54
82.16	78.35	180	4.63
83.09	78.82	190	5.15
83.99	79.23	200	5.67
84.71	79.58	210	6.06
85.57	79.90	220	6.62
86.54	80.18	230	7.34
87.33	80.42	240	7.91
88.49	80.64	250	8.87
89.49	80.83	260	9.68
89.82	81.00	270	9.82
90.07	81.15	280	9.90
89.72	81.27	290	9.42
89.15	81.39	300	8.70
88.48	81.49	310	7.90
87.76	81.58	320	7.05

87.21	81.66	330	6.37
86.86	81.73	340	5.92
86.50	81.79	350	5.45
86.68	81.84	360	5.58
87.12	81.89	370	6.01
87.57	81.93	380	6.45
87.40	81.96	390	6.22
87.05	81.99	400	5.81
86.80	82.02	410	5.50
86.36	82.04	420	5.00
85.99	82.07	430	4.56
85.44	82.09	440	3.92
85.13	82.10	450	3.56
84.78	82.12	460	3.13
84.29	82.13	470	2.56
83.93	82.14	480	2.13
83.62	82.15	490	1.75
83.25	82.16	500	1.31
83.00	82.17	510	1.00
82.97	82.18	520	0.96

Table 37: Case 10 Adapter Temperature Profile

Case 10			
Adapter Operating Temperature			
$R_{tc}^{"}$ = 0.01 [$m^2 \cdot K \cdot W^{-1}$]			
Actual [ºC]	FEM Simulation [ºC]	Time [min]	Percent Error [%]
33.28	34.14	0	2.58
34.98	35.43	10	1.28
40.51	38.58	20	4.76
43.26	41.68	30	3.64
45.43	44.53	40	1.99
47.49	47.07	50	0.88
49.68	49.31	60	0.74
52.15	51.29	70	1.64
54.45	53.03	80	2.60
55.75	54.55	90	2.15

56.79	55.90	100	1.56
57.81	57.08	110	1.26
58.64	58.12	120	0.89
59.82	59.04	130	1.30
60.70	59.84	140	1.42
61.30	60.55	150	1.22
62.04	61.18	160	1.38
62.64	61.73	170	1.46
63.55	62.21	180	2.11
64.23	62.63	190	2.49
64.68	63.01	200	2.59
65.10	63.34	210	2.71
65.61	63.63	220	3.01
66.21	63.88	230	3.52
66.95	64.11	240	4.24
67.64	64.30	250	4.94
68.97	64.48	260	6.51
69.47	64.63	270	6.96
69.70	64.77	280	7.07
69.65	64.88	290	6.85
69.17	64.99	300	6.05
68.69	65.08	310	5.26
68.19	65.16	320	4.44
67.90	65.23	330	3.93
67.57	65.29	340	3.38
67.45	65.35	350	3.11
67.66	65.40	360	3.34
68.03	65.44	370	3.80
69.01	65.48	380	5.11
68.94	65.51	390	4.97
68.52	65.54	400	4.35
68.18	65.57	410	3.83
67.72	65.59	420	3.14
67.32	65.61	430	2.54
66.97	65.62	440	2.02
66.45	65.64	450	1.22
66.26	65.65	460	0.92
65.91	65.67	470	0.36
65.67	65.68	480	0.01

65.42	65.69	490	0.41
65.06	65.69	500	0.97
64.94	65.70	510	1.17
64.96	65.71	520	1.15

BIOGRAPHICAL SKETCH

Javier E. Arroyo was born in Dallas, Texas, US on August 1, 1997. He attended Pharr-San Juan-Alamo Southwest Early College High School and graduated in 2016. He received his Bachelor of Science from the Mechanical Engineering department at the University of Texas Rio Grande Valley in December 2020. Javier continued his education at the University of Texas Rio Grande Valley and obtained his Master of Science in Engineering degree in Mechanical Engineering in May 2022. He was awarded the Mechanical Engineering Graduate Outstanding Student Award during the Spring 2022 semester. Javier was awarded the David Dwight Eisenhower Fellowship Transportation Program three consecutive years and several other academic scholarships. Javier served as the Lead Manufacturing and Testing Engineer for the UTRGV Baja Racing Team for the 2017-2020 competition years and the Graduate Advisor for the Mini Baja Racing Team at UTRGV for the 2021-2022 competition year. He will continue his higher education career pursuing his Doctoral Degree in Mechanical Engineering at the University of Nebraska-Lincoln. Javier Arroyo can be reached at j.arroyojr5@gmail.com.